

Incorporation of Europium Into GaN Nanowires by Ion Implantation

Djibril Nd Faye, Xavier Biquard, Emilio Nogales, Miguel Felizardo, Marco Peres, Andrés Redondo-Cubero, Thomas Auzelle, Bruno Daudin, Luiz H.G. Tizei, Mathieu Kociak, Pierre Ruterana, Wolfhard Moeller, Bianchi Mendez, Eduardo Alves, and Katharina Lorenz

J. Phys. Chem. C, **Just Accepted Manuscript** • DOI: 10.1021/acs.jpcc.8b12014 • Publication Date (Web): 02 Apr 2019

Downloaded from <http://pubs.acs.org> on April 3, 2019

Just Accepted

“Just Accepted” manuscripts have been peer-reviewed and accepted for publication. They are posted online prior to technical editing, formatting for publication and author proofing. The American Chemical Society provides “Just Accepted” as a service to the research community to expedite the dissemination of scientific material as soon as possible after acceptance. “Just Accepted” manuscripts appear in full in PDF format accompanied by an HTML abstract. “Just Accepted” manuscripts have been fully peer reviewed, but should not be considered the official version of record. They are citable by the Digital Object Identifier (DOI®). “Just Accepted” is an optional service offered to authors. Therefore, the “Just Accepted” Web site may not include all articles that will be published in the journal. After a manuscript is technically edited and formatted, it will be removed from the “Just Accepted” Web site and published as an ASAP article. Note that technical editing may introduce minor changes to the manuscript text and/or graphics which could affect content, and all legal disclaimers and ethical guidelines that apply to the journal pertain. ACS cannot be held responsible for errors or consequences arising from the use of information contained in these “Just Accepted” manuscripts.



SCHOLARONE™
Manuscripts

1
2
3
4
5
6
7
8
9
10
11
12
13
14
15
16
17
18
19
20
21
22
23
24
25
26
27
28
29
30
31
32
33
34
35
36
37
38
39
40
41
42
43
44
45
46
47
48
49
50
51
52
53
54
55
56
57
58
59
60

Incorporation of Europium into GaN Nanowires by Ion Implantation

D. Nd. Faye¹, X. Biquard², E. Nogales³, M. Felizardo¹, M. Peres¹, A. Redondo-Cubero¹⁺, T. Auzelle^{4,5}, B. Daudin⁴, L.H.G. Tizei⁵, M. Kociak⁵, P. Ruterana⁶, W. Möller⁷, B. Méndez³, E. Alves¹, K. Lorenz^{1,8*}

¹*IPFN, Instituto Superior Técnico, Universidade de Lisboa, Campus Tecnológico e Nuclear, Estrada Nacional 10, 2695-066 Bobadela LRS, Portugal*

²*Univ. Grenoble Alpes, CEA, INAC-MEM, 38000 Grenoble, France*

³*Departamento de Física de Materiales, Universidad Complutense, 28040 Madrid, Spain*

⁴*Univ. Grenoble Alpes, CEA, INAC-Phelqs, 38000 Grenoble, France*

⁵*Laboratoire de Physique des Solides, Université Paris-Sud, CNRS-UMR 8502, Orsay 91405, France*

⁶*Centre de recherche sur les Ions les Matériaux et la Photonique (CIMAP) ENSICAEN, Boulevard Maréchal Juin 14050 Caen France*

⁷*Helmholtz-Zentrum Dresden-Rossendorf, Institute of Ion Beam Physics and Materials Research, Bautzner Landstraße 400, D-01328 Dresden, Germany*

⁸*Instituto de Engenharia de Sistemas de Computadores- Microsistemas e Nanotecnologias (INESC-MN), Rua Alves Redol 9, 1000-029 Lisboa, Portugal*

⁺ Current address: Departamento de Física Aplicada y Centro de Micro-Análisis de Materiales, Universidad Autónoma de Madrid, Madrid, Spain

^{*} Tel. +351-219946052; fax +351 21 9946285; lorenz@ctn.tecnico.ulisboa.pt

ABSTRACT

Rare earth (RE) doped GaN nanowires (NWs), combining the well-defined and controllable optical emission lines of trivalent RE ions with the high crystalline quality, versatility and small dimension of the NW host, are promising building blocks for future nanoscale devices in optoelectronics and quantum technologies. Europium doping of GaN NWs was performed by ion implantation and structural and optical properties were assessed in comparison to thin film reference samples. Despite some surface degradation for high implantation fluences, the NW core remains of high crystalline quality with lower concentrations of extended defects than observed in ion implanted thin films. Strain introduced by implantation defects is efficiently relaxed in NWs and the measured deformation stays much below that in thin films implanted in the same conditions. Optical activation is achieved for all samples after annealing and, while optical centres are similar in all samples, Eu^{3+} emission from NW samples is shown to be less affected by residual implantation damage than for the case of thin films. The incorporation of Eu in GaN NWs was further investigated by nano-cathodoluminescence and X-ray absorption spectroscopy (XAS). Maps of the Eu-emission intensity within a single NW agree well with the Eu-distribution predicted by Monte Carlo simulations suggesting that no pronounced Eu-diffusion takes place. XAS shows that 70-80% of Eu is found in the 3+ charge state while 20-30% is 2+ attributed to residual implantation defects. A similar local environment was found for Eu in NWs and thin films: for low fluences, Eu is mainly incorporated on substitutional Ga-sites while for high fluences XAS points at the formation of a local EuN-like next neighbour structure. Results reveal the high potential of ion implantation as a processing tool at the nano-scale.

INTRODUCTION

1
2
3 Rare earth doped GaN thin films have been the subject of intense research in the
4
5 past two decades due to their promising properties for optoelectronic and spintronic
6
7 applications¹. In particular, doping with europium led to the demonstration of the first
8
9 low voltage GaN:Eu light emitting diode (LED)². The typical red luminescence of the Eu³⁺
10
11 ions is of particular interest since the efficiency of conventional III-nitride LEDs drops
12
13 significantly in the green and red spectral region³. While GaN:Eu films have been
14
15 fabricated by various techniques such as in-situ doping during molecular beam epitaxy
16
17 (MBE)⁴ and metal organic vapor phase epitaxy (MOVPE)² or ex-situ doping by ion
18
19 implantation^{5,6}, studies on Eu-doped GaN nanowires (NWs) are still scarce^{7,8,9}. Given the
20
21 demonstrated advantages of GaN NWs (for example grown by MBE) over epitaxial films,
22
23 including low dislocation densities, their ability of efficient strain relaxation even on
24
25 lattice mismatched substrates and improved light extraction¹⁰, functionalization of
26
27 these NWs with optically active ions could lead the way to new applications and device
28
29 designs. However, in-situ doping of nanowires is challenging due to frequently occurring
30
31 segregation of second phases or morphology changes. Furthermore, so called self-
32
33 purification processes cause the expulsion of dopants from the bulk of the NWs to their
34
35 surface. Aravindh and Roqan, based on density functional theory (DFT) calculations,
36
37 suggest that the most likely incorporation sites of the rare earth Gd in GaN NWs are at
38
39 the surface¹¹. Xu et al.⁷ fabricated Eu-doped GaN nano-needles via a vapor transport
40
41 route with the dominant Eu³⁺ emission line, corresponding to the ⁵D₀→⁷F₂ intra-atomic
42
43 transition, at 611 nm. Typical wavelengths for the main line of various optically active
44
45 Eu³⁺ centers in GaN:Eu films lie in the range from 618 to 625 nm¹². The large shift of the
46
47 emission to higher energy for the case of the nano-needles can be attributed to surface
48
49 effects⁷. Confinement effects should play a negligible role in this behavior since only
50
51
52
53
54
55
56
57
58
59
60

1
2
3 minor shifts due to site multiplicities or different strain states were reported for rare
4
5 earths incorporated in quantum dots and NWs^{13,14}. Sekiguchi et al.⁹, reported the Eu-
6
7 doping of GaN NWs during MBE growth leading to similar optical centers as in thin films
8
9 while exhibiting strongly reduced concentration quenching. Despite these highly
10
11 promising results, doping led to morphology changes and even polycrystalline growth
12
13 for high Eu concentrations⁹. Ion implantation was suggested as a promising alternative
14
15 to introduce dopants in NWs without affecting their morphology^{15,16}. Indeed,
16
17 establishing the ion implantation technique as processing tool at the nanoscale could
18
19 facilitate the use of doped NWs as building blocks for future nanodevices in electronics
20
21 and photonics. Rodrigues et al.⁸ studied Eu implantation in GaN NWs using fluences of
22
23 5×10^{13} and 3×10^{15} at/cm² and incidence angles with respect to the c- axes of the
24
25 vertically aligned NWs of 20 and 30°. It was shown that annealing leads to effective
26
27 optical activation of the Eu³⁺ emission with higher intensity and reduced temperature
28
29 quenching compared to GaN films prepared in the same conditions. Furthermore, the
30
31 dominant optical center is the same in NWs and films and no significant changes were
32
33 seen in the spectral shape for different fluences and implantation geometries⁸.
34
35
36
37
38
39
40
41

42 Nevertheless, ion implantation is inherently connected with defects created by
43
44 the bombardment with heavy and energetic ions which can deteriorate structural and
45
46 optical properties. Implantation damage build-up processes in GaN thin films are
47
48 relatively well understood. In particular, they are dominated by strong dynamic
49
50 annealing which leads to the efficient recombination of point defects already during the
51
52 implantation but also promotes the formation of thermally stable extended defects such
53
54 as point defect clusters and stacking faults^{17,18,19,20}. Only few studies address
55
56 implantation damage mechanisms in GaN NWs^{21,22,23,24}. Molecular dynamics simulations
57
58
59
60

1
2
3 for Er implanted GaN NWs reveal high sputtering yields and an accumulation of defects
4
5 close to the surface²⁴. High sputtering yields and surface defects are furthermore
6
7
8 consistent with the experimental observation of blisters at the surface of GaN NWs after
9
10 implantation²². Both simulations²⁴ and experiments²³ reveal the introduction of
11
12 hydrostatic strain by the implantation defects. In contrast, other experimental studies
13
14 suggest increased dynamic annealing in GaN NWs as compared to bulk material²¹ and
15
16 for the special case of Pr implanted GaN NWs, Pr related luminescence was even
17
18 enhanced by the interaction with certain defects created by the implantation and
19
20 annealing processes²³. Thermal annealing of implantation damage is challenging in GaN
21
22 due to the thermal dissociation of the crystal starting at approximately 800 °C²⁵. This
23
24 issue is aggravated for the case of NWs due to the increased surface area to volume ratio.
25
26 The application of special capping layers or annealing under high nitrogen pressure,
27
28 successful in GaN layers^{26,27}, are not practical for NWs. Nevertheless, it was shown that
29
30 rapid thermal annealing at 1000 °C can effectively reduce implantation damage and
31
32 optically activate rare earth ions^{8,23}.
33
34
35
36
37
38
39

40 In this work we report a comprehensive study of the structural alterations, in
41
42 particular strain and morphology changes, induced by implantation of GaN NWs.
43
44 Furthermore, we advance a microscopic model for the incorporation of implanted Eu in
45
46 GaN NWs and thin films.
47
48
49
50
51
52
53
54
55
56
57
58
59
60

METHODS

Vertically aligned GaN NWs have been grown by molecular beam epitaxy on (111) Si substrates using a thin (2-3 nm) AlN buffer layer. The NW growth was performed for ~13 hours at 800 °C in nitrogen rich conditions; details were published previously²⁸. Active N flux was provided by a radio frequency N₂ plasma cell and Ga flux by a standard effusion cell. N-rich conditions were used, i.e. a Ga/active N flux ratio of about 1/3. Deoxidation of the (111) Si substrate was performed by dipping in a 15%-HF: deionized water bath, followed by a smooth annealing in vacuum at 300 °C and next at 900 °C till reflection high energy electron diffraction (RHEED) observation of a clear 7 × 7 reconstruction, indicative of a clean surface²⁸.

Figs. 1a-d show scanning electron microscopy (SEM) images of the as-grown GaN NWs for sample set 1 revealing an average diameter of ~50 nm close to the center of the wafer (Fig. 1a and b) and ~100 nm towards the periphery (Fig. 1c and d) leading to increasing coalescence when approaching the edge of the wafer. The NW length varied between 2000 and 2500 nm and the NW density ranged from 2 to 7 × 10⁹ cm⁻² increasing towards the wafer edge. In the zones of low NW density close to the center, a 2D layer, consisting of coalesced GaN pyramids²⁸, is visible at the base of the NWs (Fig. 1a).

A second set of samples, specially designed for the synchrotron measurements, showed a more homogeneous NW density of 9 × 10⁹ cm⁻² across the wafer and no 2D layer (Figs. 1e and f).

Samples were implanted at room temperature with 300 keV Eu ions to fluences ranging from 1 × 10¹³ at/cm² to 5 × 10¹⁵ at/cm². Some preliminary results for implantation at 600 °C are also discussed. The implantation was done in six steps rotating the sample sixty by sixty degrees in the azimuthal angle while the incidence angle between the beam and the NW axes was 20° for sample set 1 and 40° for sample set 2. This procedure yields a distribution of Eu and implantation defects which is close to rotationally symmetric around the central axis of the NWs and prevents the NWs from bending due to strain

1
2
3 gradients. The final Eu distribution inside the NWs is complex and depends on the
4 implantation angle, NW diameter and NW density. The three dimensional distribution
5 of Eu and defects has been studied using Monte Carlo simulations implemented in the
6 TRI3DYN code^{29,30,31}. This code is based on the binary collision approximation and allows
7 simulating dynamic effects of ion irradiation in three dimensional structures.
8
9
10
11

12
13 Annealing of the samples was performed for holding times of 30 s at 1000 °C with a
14 heating ramp of 30 °C per second in an ANNEALSYS halogen lamp rapid thermal
15 processor under flowing nitrogen.
16
17

18
19 In all cases, thick (~3 μm) GaN layers (purchased from Lumilog) grown by metal organic
20 chemical vapor deposition on (0001) sapphire were implanted and annealed
21 simultaneously for comparison. Additionally, a reference layer for extended X-ray
22 absorption spectroscopy (EXAFS) measurements was implanted along the c-axis to a low
23 fluence of 1×10^{14} at/cm² and annealed in optimized high temperature high pressure
24 (HTHP) conditions of 1400 °C and nitrogen pressure of 1 GPa³².
25
26
27
28
29

30
31 X-ray diffraction (XRD) was performed on a high resolution Bruker D8 Discover
32 diffractometer using a Göbel mirror to yield a parallel beam and an asymmetric 2-
33 bounce Ge (220) monochromator to choose the $\text{CuK}_{\alpha 1}$ line. 2θ - θ curves were acquired
34 with a 0.2 mm slit placed before the monochromator and a 0.1 mm slit in front of the
35 scintillation detector.
36
37
38
39

40
41 Conventional transmission electron microscopy (TEM) and high resolution scanning-
42 TEM (STEM) were carried out on selected samples. The NWs were dispersed on the TEM
43 grid without any further sample preparation. Conventional TEM investigations were
44 performed with a JEOL 2100 microscope and atomically resolved STEM high angle
45 annular dark field images (HAADF) have been acquired in a Nion UltraSTEM 200 both
46 operated at 200 keV.
47
48
49
50

51
52 Cathodoluminescence (CL) spectroscopy was carried out at room temperature using a
53 Hitachi S2500 SEM and a Hamamatsu PMA-11 charge coupling device camera. The
54 acceleration voltage was $V_{\text{acc}} = 5$ kV yielding an electron penetration depth in GaN of
55 ~70 nm as estimated by the Monte Carlo code CASINO³³. The beam was defocused to
56 several hundreds of micrometers diameter in order to limit the excitation density and
57
58
59
60

1
2
3 mitigate the strong intensity quenching of the Eu^{3+} lines observed for a focused beam.
4
5 The electron beam hits both the top surface and parts of the side facets of the NWs with
6
7 an incidence angle of 25° towards the surface normal. Selected NW samples were
8
9 furthermore analyzed using nano-CL on single NWs in a STEM (VG HB501) operated with
10
11 80 keV electrons (typical electron current 60 pA) with the sample kept at 150 K³⁴.
12

13 X-ray Absorption Spectroscopy (XAS) measurements were conducted on both FAME
14 (BM30B) and SPLINE (BM25) beamlines at the European Synchrotron Radiation Facility
15 (ESRF) in Grenoble, France. The main optical element of both beamlines is a two-crystal
16 monochromator (Si (220) for FAME and Si (111) for SPLINE) with a cooled first crystal
17 and a sagittally bent second crystal^{35,36,37}. Two bendable Rh-coated mirrors located
18 before and after the monochromator ensure harmonics rejection. XAS spectra were
19 recorded at the L_{III} edge of Eu (6977 eV) in fluorescence mode with a multi-element
20 energy-resolved Ge detector. Experiments were conducted at room temperature except
21 for the very low fluence GaN film reference sample which was measured at 100 K to
22 benefit from an increased signal-to-noise ratio that compensates for the very low
23 amount of implanted Eu. The energy calibration was made using a Fe reference foil
24 (7112 eV). Measurements were performed in grazing incidence geometry (with an angle
25 of $\sim 5\text{-}15^\circ$ between the beam and the sample surface) in order to maximize the signal
26 from the implanted layer. Base line extraction of XAS spectra as well as EXAFS analysis
27 were conducted using the well-known DEMETER comprehensive system for processing
28 and analyzing XAS data (that includes *ATHENA*, *ARTEMIS* and *IFEFFIT programs*)³⁸. For
29 meaningful quantification, we took into account the polarization of the X-ray beam.
30 Further details on XAS measurements and data analysis are given in the supplementary
31 materials.
32
33
34
35
36
37
38
39
40
41
42
43
44
45
46
47
48
49
50
51
52
53
54
55
56
57
58
59
60

RESULTS AND DISCUSSION

1. Dynamic Monte Carlo simulations

TRI3DYN simulations have been performed for three relevant configurations: implantation of Eu at 20° tilt into NW arrays with either i) 50 nm diameter and an areal density of $2 \times 10^9 \text{ cm}^{-2}$ or ii) 100 nm diameter and an areal density of $7 \times 10^9 \text{ cm}^{-2}$ (corresponding to sample set 1 with samples from the center or the edge of the wafer, respectively) and iii) implantation at 40° tilt into NW arrays with 100 nm diameter and an areal density of $9 \times 10^9 \text{ cm}^{-2}$ (corresponding to sample set 2 used for XAS measurements). A regular two-dimensional square configuration of the nanowires with the desired areal density is modelled by the choice of periodic lateral boundary conditions. For rotational symmetry around the axis of the nanowires, the structure is randomly rotated at each ion incidence. An extended description of the simulation, including the choice of critical parameters, is included in the Supplementary Information. Besides the ion energy and NW diameter, the implantation geometry and NW density will determine the distribution of Eu in the NWs due to shadowing effects by neighboring NWs. All results are shown for a final fluence of $3 \times 10^{15} \text{ at/cm}^2$. Fig. 2 shows the simulated elemental distributions (Ga, N, Eu) in a longitudinal slice of 8 nm thickness along the NW length for cases i) and ii). Note that for case ii) in the simulation a NW length of 1000 nm was assumed allowing a better lateral resolution and saving computational costs. Fig. 2 also gives the distribution of implantation damage given in displacements per atoms (dpa). For case i) (low density of 50 nm diameter NWs), implantation yields an almost homogeneous distribution of Eu along the entire length of the wire. A slightly higher Eu concentration is found at a depth of $\sim 55 \text{ nm}$ corresponding to ions that enter the NW from the top surface. This is seen better in Fig. 3 showing the average Eu-concentration along the NW length for the three cases. Accordingly, the implantation damage for case i) is also distributed homogeneously along the entire NW with some increased displacements close to the upper surface due to ions entering the NW from the top. According to the simulations, for this low density of NWs only about 54% of all ions are stopped within the NWs while the remaining 46% are implanted into the Si-substrate. Indeed, RBS spectra on the template after removing

1
2
3 the NWs by scratching and ultrasound cleaning showed that a large fraction of Eu was
4 implanted into the substrate and 2D layer in samples with low NW density. For case ii)
5 (high density of 100 nm diameter NWs - see bottom row of Fig. 2), the distribution of Eu
6 and implantation damage is less homogeneous. A large fraction of ions enters the NWs
7 through the top surface leading to an increased Eu concentration in the first ~100 nm of
8 the NW (Fig. 3) as well as to increased lattice damage close to the NW tip similar to
9 implantation in planar substrates. For these implantation conditions simulations show
10 that 98.6% of all ions are stopped within the first 1000 nm of the NW (see Fig. 3). Most
11 ions entering through the lateral surface will not reach the NW center due to the higher
12 NW diameter for case ii) and Eu as well as defects will accumulate close to the rim of the
13 NWs. The lateral distribution of Eu is shown in Fig. 4 where the top row shows an
14 integration over the first 50-150 nm of the NW tip where the Eu distribution is
15 influenced by ions entering via the top surface leading to an almost homogeneous
16 distribution of Eu. For integration over the remaining NW base (bottom row of Fig. 4)
17 the Eu distribution is determined by ions entering the NW from the side facets. For the
18 50 nm diameter NWs this leads to a maximum Eu concentration close to the central axis
19 of the NW while for the 100 nm diameter NWs the doping concentration is higher close
20 to the side facets and decreases towards the central axis.
21
22
23
24
25
26
27
28
29
30
31
32
33
34
35

36
37 For optical measurements and XRD, Eu reaching the silicon substrate does not interfere
38 with the signal from the NWs (note that Eu is optically inactive in Si). However, for XAS
39 measurements it is important to avoid any Eu reaching the substrate since all Eu ions
40 will contribute to the measured signal. Therefore, the second set of samples was
41 implanted using an incident angle of 40°. This geometry, together with the high and
42 homogeneous density of NWs and the absence of a 2D layer, assured that Eu was only
43 implanted into the GaN NWs and not into the Si-substrate or the coalesced GaN 2D layer
44 at the base of the NWs. Fig. 3 clearly shows that the Eu distribution is concentrated in
45 the top 500 nm of the NWs. In fact, the simulations indicate that 99.3% of all ions come
46 to rest inside the NWs while the remaining 0.7% are being backscattered.
47
48
49
50
51
52
53
54
55

56 An additional feature observed in the elemental maps in Fig. 2 is a preferential loss of
57 nitrogen due to sputtering, leading to a slight N-deficiency in the bulk of the NW, in
58 particular, in the regions of higher damage concentration. This is in agreement with
59
60

1
2
3 Molecular Dynamics simulations of ion implantation in GaN NWs³⁹. A slight enrichment
4 in N is observed at the outer surface, which is attributed to the redeposition of
5 preferentially sputtered N atoms from the surrounding nanowires.
6
7

8 9 **2. Strain and morphology**

10
11
12 Fig. 5 shows XRD (0004) 2θ - θ curves for the first set of NWs and films implanted to
13 different fluences of 300 keV Eu ions at 20° incidence. For the thin film reference
14 samples, the implantation leads to the formation of a satellite peak at lower 2θ angle
15 than the main Bragg peak clearly visible for the lowest fluence. The hydrostatic strain
16 caused by implantation defects leads to an expansion of the c-lattice parameter within
17 the implanted volume as it was first reported by Liu et al. for c-plane GaN layers⁴⁰. With
18 increasing fluence the induced strain increases and the satellite peak shifts to lower
19 angles. For fluences starting from 5×10^{14} at/cm², the diffraction intensity of the satellite
20 peak decreases strongly and XRD becomes insensitive to further defect formation.
21
22 Similar curves have been reported for Eu implantation along the c-axis of GaN except
23 that the saturation regime, when the diffraction pattern does not evolve further, is only
24 reached at higher fluences (1×10^{15} at/cm²)⁴¹. This saturation was attributed to the
25 formation of a dense network of extended defects leading to plastic deformation and
26 strain relaxation. Many authors have reported similar strain formation in GaN for
27 different implantation conditions^{42,43,44}. In fact, it was suggested that strain induced by
28 implantation defects is the driving force behind the defect mobility and dynamic
29 annealing in GaN leading to the change of defect microstructure as the fluence
30 increases⁴⁵. Detailed XRD studies on GaN NWs and NW heterostructures showed that,
31 due to their vertical alignment, NWs can be studied by laboratory XRD in a similar way
32 as planar heterostructures^{46,47}. However, the diffraction intensity is strongly reduced
33
34
35
36
37
38
39
40
41
42
43
44
45
46
47
48
49
50
51
52
53
54
55
56
57
58
59
60

1
2
3 due to the reduced sample volume and the fact that, due to the relatively high tilt
4
5 between NWs, only a fraction of them will be well-oriented to satisfy the Bragg condition
6
7 and contribute to the Bragg peak intensity. Moreover, the line shape and broadening
8
9 are influenced by the inclination of the NWs normal to the scattering plane and
10
11 inhomogeneous fluctuating strain⁴⁷. Indeed, the XRD patterns of the as-grown NWs (see
12
13 Fig. 5a) show the typical non-Gaussian peak broadening which Kaganer et al. attributed
14
15 to random distortions caused by lattice defects at the interface between the NWs and
16
17 the substrate and at joints between coalesced NWs⁴⁷. Nevertheless, similar to the layers,
18
19 a second peak formed after implantation is clearly visible, which is strongly overlapped
20
21 to the Bragg peak arising from unimplanted GaN. Two main differences can be pointed
22
23 out when comparing these diffraction patterns to those of the thin film reference
24
25 samples. First, the satellite peaks in NWs have a comparable intensity as the peak
26
27 corresponding to unimplanted volume. This can be understood by the fact that the ratio
28
29 of implanted/unimplanted volume in the NWs is much larger since not only a thin
30
31 surface layer is doped but ions can enter through the side facets of the wires and
32
33 penetrate the entire wire width. Like this, only the bases of the NWs remain
34
35 unimplanted due to shadowing by the surrounding NWs. It is worth mentioning that we
36
37 did not see any significant difference in the XRD patterns from the wafer center or the
38
39 peripheries suggesting that the 2D layer present in sample set 1 has a similar behavior
40
41 as the NWs. Second and more importantly, the maximum strain that is reached is much
42
43 lower in the NWs than in the thin films (see upper x-axis in Fig. 5 where the angle was
44
45 converted to perpendicular strain as $\varepsilon^\perp = (c_{exp} - c_0)/c_0$, with c_0 the c -lattice
46
47 parameter of the as-grown GaN and c_{exp} the expanded c -lattice parameter as
48
49 determined from the 2θ position of the XRD curves). While in thin films already for the
50
51
52
53
54
55
56
57
58
59
60

1
2
3 lowest fluence the incorporated perpendicular strain exceeds 0.5%, this value is never
4
5 reached in the NWs even for the highest investigated fluence. The lower strain state in
6
7 NWs can be attributed to more efficient relaxation mechanisms in low dimensional
8
9 structures especially since implantation defects in NWs are expected to accumulate at
10
11 the surface. The higher vacancy concentration (relative to interstitial defects) suggested
12
13 by molecular dynamics simulations may also play a role²⁴. Furthermore, it is possible
14
15 that a biaxial component of defect induced strain increases the perpendicular strain in
16
17 bulk material due to the in-plane stress imposed by the unimplanted bulk⁴⁸ while in NWs
18
19 the a -lattice parameter is freer to expand. Strain in the c -plane is indeed predicted to
20
21 occur by molecular dynamics simulations although with lower magnitude than the
22
23 perpendicular strain²⁴. Unfortunately, it was not possible to measure the a -lattice
24
25 constant in the present work due to the small material volume in NW samples and the
26
27 low intensity of the asymmetric XRD reflections. Synchrotron diffraction measurements
28
29 should be done to clarify this point.
30
31
32
33
34
35
36
37

38 The effect of annealing on XRD 2θ - θ curves is shown in Fig. 6 for the NW samples
39
40 implanted with 40° tilt and annealed at 1000°C . In agreement with the Monte Carlo
41
42 simulations showing that only the upper part of the NWs is implanted in this geometry,
43
44 the intensity ratio of the diffraction peaks corresponding to implanted and virgin
45
46 material is lower than for sample set 1. After annealing the curves become symmetric
47
48 and resemble those of the as-grown samples suggesting that the defect induced strain
49
50 is efficiently removed even for the highest fluence of 5×10^{15} at/cm². Although direct
51
52 comparison of the curves should be done with caution due to lateral inhomogeneities
53
54 of the samples, a slight broadening of the curves for the annealed NWs implanted to the
55
56
57
58
59
60

1
2
3 highest fluences is probably due to remaining implantation defects and surface
4
5 degradation.
6

7
8
9 For thin film samples efficient strain recovery is only seen for the lowest fluence of
10
11 1×10^{13} at/cm²; for higher fluences it is not even achieved after annealing at 1450 °C as
12
13 reported previously and diffraction curves remain asymmetric after annealing^{32,49}.
14

15
16
17 There is no significant difference between the XRD results on samples implanted with
18
19 20° and 40° tilt. We recently showed that the defect structures in thin films strongly
20
21 depend on the surface orientation (a-plane, c-plane or m-plane)⁵⁰, however, the
22
23 influence of the exact implantation geometry and its impact on damage in NWs needs
24
25 further investigations.
26
27

28
29
30 The morphology changes upon implantation were investigated by TEM for the different
31
32 fluences. Up to a fluence of 5×10^{14} at/cm² no significant change has been noticed in the
33
34 NW morphology (Fig. 7a). All the nanowires exhibit well defined clean facets and no
35
36 amorphization. Their diameter progressively decreases towards the top which is
37
38 probably due to the growth process. At this fluence, the nanowire may exhibit one or
39
40 two basal stacking faults⁵¹ across the entire width (marked with white arrows in Fig. 7b).
41
42 Such defects are probably generated by the ion implantation; indeed they are known to
43
44 constitute the basic deformation channel for GaN thin films during such an implantation
45
46 process¹⁹. By the fluence of 1×10^{15} at/cm², two types of structural changes are seen to
47
48 take place in the nanowires. As can be seen in Fig. 7c, nanowires can bend at the level
49
50 of the tip (T), but also at their base (B), and this can be accompanied by rounding at the
51
52 tips. However, at this fluence, most of the observed nanowires stay upright as shown by
53
54 the weak beam image recorded with $g = 0002$ (Fig. 7d). The exhibited contrast indicates
55
56
57
58
59
60

1
2
3 that, although the nanowire has been damaged, the core retains a crystalline structure,
4
5 all along the nanowire. This is also visible through the lattice fringes which disappear
6
7 towards the outer part of the wire which then displays a random contrast indicating that
8
9 this area has undergone amorphization. This is in contrast with our earlier reports on
10
11 bulk GaN where up to the highest fluences the material was shown to transform to
12
13 nanocrystalline form instead of becoming amorphous under ion implantation⁵². For this
14
15 fluence and beyond, the formation of surface defects such as blisters (Fig. 7e) is
16
17 consistent with the high sputtering yields suggested by molecular dynamics
18
19 simulations²⁴ and previous experimental results²². For the highest fluence
20
21 (3×10^{15} at/cm²), only a limited number of NWs retain their integrity when transferred
22
23 to the TEM grid for observation (Fig. 7f); in this case the rounding of the tips is more
24
25 prominent and more stacking faults can be seen in the less damaged parts of the NWs
26
27 (Fig. 7g). Nevertheless, compared to GaN epitaxial layers, the density of stacking faults
28
29 is very small, which means that the formation of such defects is not the dominant
30
31 mechanism in these low dimensional structures. At this fluence, most of the nanowires
32
33 become brittle leading to the easy breaking-off of the top which is the most sollicitated
34
35 part of the NWs when they are transferred to the TEM grid (Fig. 7h).

36
37
38 After annealing at 1000 °C, scanning TEM (STEM) high angle annular dark field (HAADF)
39
40 was carried out as shown in Fig. 8 for a NW implanted with 1×10^{15} at/cm². As can be
41
42 seen in Fig. 8a, the nanowire surface is no longer limited by large and regular
43
44 crystallographic faces. In this low magnification micrograph, the roughness is clearly
45
46 visible on the sides and influences the contrast of the whole image as indicated by the
47
48 darker spots which reveal that the corresponding thickness is smaller than that of the
49
50 surrounding areas. Most interesting, as shown in figure 8b, the amorphous parts as well
51
52
53
54
55
56
57
58
59
60

1
2
3 as the surface blisters have completely disappeared, which means that the amorphous
4
5 areas may have recrystallized during the annealing process or evaporated. All along the
6
7 annealed nanowire, no basal stacking faults can be seen anymore, which is an indication
8
9 that they have been removed. Only in very few areas, however, some local irregular
10
11 features have been noticed (Figs. 8c and d) which may correspond to small extended
12
13 defects possibly consisting of three extra planes. This behavior is still under investigation.
14
15
16
17

18 **3. Optical activation**

20
21 Despite the pronounced surface degradation but consistent with the high crystalline
22
23 quality of the NW core, where most of the Eu ions should come to rest, all samples show
24
25 optical activation of the Eu³⁺ ions with the dominant line, corresponding to the ⁵D₀→⁷F₂
26
27 transition, at ~622 nm. The inset in Fig. 9b presents the CL spectra of a NW and a thin
28
29 film sample both implanted to a fluence of 1×10¹⁴ at/cm². The spectra are representative
30
31 for all fluences and confirm that the Eu³⁺ optically active centers are similar in NWs and
32
33 thin films. This is in agreement with the detailed photoluminescence spectroscopy study
34
35 performed on a sub-set of the samples studied here and which showed that the
36
37 dominant Eu³⁺ center is the same in NWs and films despite a small shift in the line
38
39 positions presumably due to different strain states of the GaN hosts⁸. These
40
41 observations were independent of implantation fluence and geometry. In the following
42
43 we focus on the emission intensity. The CL intensity of the main Eu³⁺ emission line at
44
45 622 nm is plotted in Fig. 9 for NWs (a) and thin films (b) as a function of the fluence. The
46
47 values were achieved by measuring three spectra in different points of the sample,
48
49 which varied only slightly, and averaging the measured intensities. For the NW sample
50
51 this was done in two regions with high and low NW density. For the case of the doped
52
53
54
55
56
57
58
59
60

1
2
3 thin films (Fig. 9b) the intensity first increases with the fluence up to 5×10^{14} at/cm² and
4
5 then decreases again due to the severe lattice damage which could not be removed by
6
7 thermal annealing. This behavior is similar to that observed previously for implantations
8
9 performed along the c-axis. However, in the latter case the decrease of intensity only
10
11 occurs at higher fluences⁵³ which can be attributed to the lower damage level when
12
13 implantation is performed in channelling geometry (which promotes the steering of ions
14
15 along the atomic rows and reduces the direct collisions with the target nuclei)^{42,54}. For
16
17 the case of the NWs, distinct behaviours are observed for regions with high or low NW
18
19 density. For low NW density a saturation of the emission for high fluences is observed.
20
21 Although no pronounced intensity decrease occurs as for the thin films, the similar
22
23 behaviour might suggest that a large fraction of Eu was implanted into the 2D layer at
24
25 the base of the NWs and with a similar behaviour as that observed for thin films. For
26
27 high NW density, on the other hand, no saturation or quenching is observed up to the
28
29 highest measured fluence. However, the increase of emission intensity is much lower
30
31 than expected when assuming a direct proportionality between Eu concentration and
32
33 emission intensity. This implies that most of the implanted Eu ions in high fluence
34
35 samples are not optically active. This can be either due to a less effective energy transfer
36
37 from the GaN host to the Eu³⁺ ions, the quenching of luminescence due to the formation
38
39 of defects acting as non-radiative recombination centres or due to the incorporation of
40
41 Eu in inadequate lattice sites, for example sites which do not support the 3+ valence
42
43 state of the Eu ions.
44
45
46
47
48
49
50
51
52
53

54
55 In order to get a more microscopic view of Eu incorporation in NWs, nano-CL was
56
57 performed on single NWs as presented in Fig. 10. Fig. 10a shows the CL spectra acquired
58
59 at different positions along the NW lengths in the seven regions indicated in the TEM
60

1
2
3 image of Fig. 10b. Eu emission at 622 nm is clearly observed within the first 1000 nm
4
5 from the top. This is in good agreement with the Monte Carlo simulations showing that
6
7 most Eu ions come to rest in this region for high NW density. At the bottom part of the
8
9 NW only broader bands at ~ 400 and ~ 570 nm are observed. Emission at 400 nm was
10
11 also observed in PL spectra of the as-grown samples and attributed to donor acceptor
12
13 pair transitions while the yellow emission was formed after implantation/annealing and
14
15 attributed to defects⁸. In the present case, the yellow luminescence in spectra 5, 6 and
16
17 7 may be due to defects created by sputtered atoms or surface defects created during
18
19 annealing. Figs. 10c and d show maps of the luminescence intensity from the same NW
20
21 integrating the region from 350 to 550 nm (Fig. 10c), corresponding mainly to DAP
22
23 emission, and integrating only the Eu^{3+} emission line at 622 nm (Fig. 10d). These maps
24
25 clearly show that Eu-emission is mainly observed at the top of the NWs. Fig. 10e presents
26
27 a more detailed luminescence map of the Eu^{3+} emission within a region corresponding
28
29 to the highest Eu concentration (marked with the larger green rectangle in Fig. 10b).
30
31 Lower Eu^{3+} emission intensity is observed at the NW edges due to both a lower probed
32
33 sample volume and low Eu concentration at the surface. Even when disregarding the
34
35 edges, Eu^{3+} emission intensity fluctuations at the nanoscale are visible. Each pixel in the
36
37 map corresponds to an area of $10 \times 10 \text{ nm}^2$. Taking into account the nanowire density,
38
39 dimension and the fluence, the number of Eu ions can be roughly estimated to be some
40
41 tens of ions per pixel. The spatial fluctuations of emission intensity can be explained by
42
43 the facts that only a small fraction of Eu ions are optically active^{55,56} as well as by the
44
45 long lifetimes of the excited Eu^{3+} states leading to a long “dark-time” of individual ions.
46
47 Furthermore, as mentioned above, ions may be incorporated into sites which do not
48
49 promote optical activity e.g. due to a valence state different from 3+.
50
51
52
53
54
55
56
57
58
59
60

4. Eu incorporation

Eu and other rare earth ions in GaN thin films are known to be preferentially incorporated in substitutional Ga-sites or slightly displaced from that site^{6,55,57,58,59,60}. Experimentally this was shown by ion channeling or emission channeling techniques which cannot be easily applied to NWs due to the low critical angles for dechanneling which are in the order of the tilt angles between individual NWs. Therefore, here we apply X-ray absorption techniques to assess the incorporation site and valence state of implanted Eu ions in NWs and thin films. Indeed, EXAFS has been successfully applied in Eu implanted and in situ doped GaN films^{61,62}. The nanoscopic nature of X-ray absorption techniques, being sensitive only to a few atomic neighbor shells around the probe atom, is ideal for the comparison of bulk material and nanostructures. A more detailed description of the data analysis can be found in the supplementary material.

Figure 11 presents the absorption spectra near the Eu L_{III} edge (X-ray absorption near edge structure (XANES) part only) for various thin film (Fig. 11a) and NW (Fig. 11b) samples after annealing. All spectra exhibit two contributions to the absorption edge corresponding to the Eu²⁺ white line at fixed energy position 6975.3 ± 0.3 eV while the line for Eu³⁺ varies from 6981.5 to 6983.1 eV. This is most visible for the thin film sample implanted with a fluence of 1×10^{15} at/cm² (RTA at 1000 °C) with Eu²⁺ and Eu³⁺ fractions of 33% and 67%, respectively. Coexistence of Eu in 2+ and 3+ oxidation states has also been reported for Eu-doped ZnO nanowires⁶³. In contrast to GaN, in the case of ZnO substitutional Eu is expected to reside in the 2+ charge state but interaction with intrinsic defects allows the stabilization in the 3+^{64,65}.

1
2
3 We observe that the Eu^{2+} contribution decreases when the fluence is lowered to
4
5 5×10^{14} at/cm² and becomes hardly visible for the HTHP annealed reference sample
6
7
8 implanted to a fluence of 1×10^{14} at/cm², which shows an Eu^{2+} fraction of only 16%. A
9
10 low Eu^{2+} fraction of 18% is also seen for NW samples implanted to a fluence as high as
11
12 1×10^{15} at/cm² provided they are implanted at 600°C. As the high implantation
13
14 temperature promotes defect mobility during the implantation, this can lead to
15
16 annihilation of defects or to increased interaction of defects among each other.
17
18

19
20
21 XANES measurements for Eu implanted directly in Si, SiO₂ and Si₃N₄ wafers revealed that
22
23 Eu in these materials is incorporated entirely in the 2+ charge state (see supplementary
24
25 material); as implantation of GaN NWs at 600 °C results in more than 80% of Eu^{3+} , this
26
27 is coherent with nano-CL results which suggested that Eu does not reach the Si substrate.
28
29 Consequently, the presence of Eu^{2+} in GaN seems to be correlated to the presence of
30
31 residual implantation defects after annealing.
32
33

34
35
36 However, the correlation of defect density and Eu^{2+} fraction is not straightforward. As
37
38 can be seen in Fig. 11 a and b, the Eu^{2+} fraction is decreasing with further increase of
39
40 fluence above 1×10^{15} at/cm² for both NW and thin film samples although the residual
41
42 defect density should be higher for these high fluence implantations. This complex
43
44 behavior shows that not simply the overall defect concentration is decisive for the Eu
45
46 charge state but also the exact defect arrangement and nature around the Eu ion.
47
48

49
50
51 It is interesting to mention that the irradiation of as-implanted (not annealed) samples
52
53 with X-rays leads to the photo-oxidation of Eu^{2+} to Eu^{3+} which induced an $\text{Eu}^{3+}/\text{Eu}^{2+}$ ratio
54
55 increase of up to 40% in 7 hours (see supplementary material for further details). For
56
57 the highest fluence of 5×10^{15} at/cm², directly after the implantation, the fraction of Eu^{2+}
58
59
60

1
2
3 is as high as 31% for thin films and 44% for NWs, and reduces after annealing to 13 and
4
5 22%, respectively. Analogously, thermal annealing leads to conversion of Eu^{2+} to Eu^{3+} .
6
7
8 The increasing $\text{Eu}^{3+}/\text{Eu}^{2+}$ ratio, caused either by thermal annealing or X-ray irradiation, is
9
10 accompanied by a better defined EXAFS signal revealing a more ordered environment
11
12 around Eu suggesting annealing of defects. Therefore, we concentrated our further
13
14 investigation on annealed samples where, within the duration of the EXAFS
15
16 measurement, no changes were seen for the case of NWs and only moderate changes
17
18 for thin film samples.
19
20
21
22

23 Inspecting the shape of the XANES curves in Fig. 11, there is a clear evolution when
24
25 decreasing the implantation fluence with a shift of the Eu^{3+} absorption edge to a lower
26
27 energy and a third feature occurring at the high energy side of the Eu^{3+} white line. Such
28
29 a change is most likely related with a local change of the Eu nearest neighbors'
30
31 coordination. This interpretation is also supported by the EXAFS results shown in Fig. 12
32
33 (for a detailed description of the EXAFS data analysis see the supplementary material).
34
35
36
37

38 Fig. 12 shows the Fourier transforms of the EXAFS spectra and fits for NW and thin film
39
40 samples implanted to different fluences after annealing at 1000 °C as well as the thin
41
42 film reference after HTHP annealing at 1400 °C. Qualitatively the results are very similar
43
44 for NWs and thin films. For the highest fluence, only the first neighbor shell (lowest R
45
46 bump around pseudo-radius $R=2 \text{ \AA}$) is visible and corresponds to light atoms,
47
48 presumably nitrogen. The second neighbor shell (expected around pseudo-radius $R=3 \text{ \AA}$)
49
50 is not visible suggesting that Eu and N in the 1st shell form a locally ordered complex
51
52 while the distortion of the crystal due to the oversized Eu (compared to Ga) and due to
53
54 implantation defects prevents a well ordered crystal structure of the 2nd shell and
55
56
57
58
59
60

1
2
3 beyond. With decreasing fluence and therefore decreasing defect density, intensity of
4 the first shell decreases, i.e. the number of N atoms in the 1st neighbor shell is reduced,
5 while the 2nd neighbor shell intensity - consisting of Ga atoms - becomes increasingly
6 visible thus revealing the ordering of the crystal structure around Eu.
7
8
9
10

11
12
13 Detailed data fitting allows further interpretation of this data. Starting with the low
14 fluence HTHP annealed reference layer, the $|\chi(R)|$ graph (see Fig. 12a) reveals at least 8
15 well defined surrounding shells below 6 Å with a maximal intensity on the second shell
16 at pseudo-radius $R=3$ Å. This demonstrates that the Eu local environment is of very good
17 crystalline quality, dominated by a second shell of heavy elements. A good fit is obtained
18 assuming 100% of the Eu incorporated on substitutional Ga-sites, i.e. with 4 nitrogen
19 atoms as nearest neighbors, 12 Ga-atoms in the second, 10 N-atoms in the third and 6
20 Ga atoms in the fourth neighbor shells. The first neighbor shell is strongly distorted (by
21 $\sim 11\%$ with an Eu-N nearest neighbor distance of 2.15 Å compared to a Ga-N nearest
22 neighbor distance of 1.94 Å in pure GaN) as expected, due to the large effective ionic
23 radius of Eu^{3+} (linearly estimated to 83.5 pm) compared to Ga^{3+} (61 pm) in tetrahedral
24 environment⁶⁶ and in good agreement with previous studies on rare earth doped GaN
25 and other III-N alloys^{61,62,67,68}. The more distant shells are found close to the expected
26 positions in undisturbed GaN (with a Eu-Ga next-nearest neighbour distance of 3.17 Å
27 compared to a Ga-Ga nearest neighbor distance of 3.18 Å in GaN). Debye-Waller factors
28 are small ($< 5 \times 10^{-3} \text{ \AA}^{-2}$ for all shells) revealing a good crystal quality. The strongly dilated
29 first neighbor shell would allow for the incorporation of more than 4 nitrogen atoms and
30 indeed leaving the number of next nearest neighbors as free fitting parameter yields
31 5.3 \pm 1.9 N as first shell without changing the goodness of the fit. It should be noted,
32 that a contribution of oxygen on the 1st nearest neighbor site cannot be discarded.
33
34
35
36
37
38
39
40
41
42
43
44
45
46
47
48
49
50
51
52
53
54
55
56
57
58
59
60

1
2
3 The graph for the lowest fluence in NWs looks qualitatively similar (see Fig. 12b) but
4 cannot be fitted assuming 100% of undisturbed substitutional Eu. The simplest model
5
6 able to satisfactorily fit the data of all samples consists of two fractions of Eu: the first
7
8 fraction corresponding to undisturbed substitutional sites, Eu_{Ga} , and the second fraction
9
10 (dominant for higher fluences and in the following named EuN-like fraction)
11
12 characterized by a local arrangement consisting of more than 4 nitrogen atoms at a
13
14 distance of $\sim 2.5 \text{ \AA}$, that is considerably larger than for Eu_{Ga} but similar to the Eu-N
15
16 distance in EuN which is 2.51 \AA ⁶⁹. Details of the fit results are given in the supplementary
17
18 material. The main conclusion is illustrated in Fig. 13 showing the fraction of
19
20 substitutional Eu_{Ga} as a function of the fluence for all analyzed samples. The
21
22 substitutional fraction is seen to decrease with implantation fluence and is typically
23
24 lower for NW samples than for thin film samples. For the highest fluence in thin films
25
26 and NWs this fraction approaches zero and all Eu ions are found in EuN-like environment.
27
28 The figure shows furthermore that the as-implanted NWs ($1 \times 10^{15} \text{ at/cm}^2$) show slightly
29
30 higher substitutional fractions than after annealing which is consistent with ion
31
32 channeling data on ion-implanted thin films and probably due to defect diffusion and
33
34 trapping during annealing⁵³.

35
36 Although the $1 \times 10^{15} \text{ at/cm}^2$ (RTA @1000 °C) NW sample implanted at 600 °C reveals a
37
38 higher $\text{Eu}^{3+}/\text{Eu}^{2+}$ ratio than for implantation at room temperature the Eu_{Ga} substitutional
39
40 fraction drops to zero. The higher mobility of defects during implantation at elevated
41
42 temperatures seems to favor the formation of EuN-like complexes. This is consistent
43
44 with the XANES spectral shape which resembles that of high fluence implanted samples
45
46 (see Fig. 11).
47
48
49
50
51
52
53
54
55
56
57
58
59
60

1
2
3 On first sight, the change of preferential incorporation site from Eu_{Ga} for low fluences to
4
5
6
7
8
9
10
11
12
13
14
15
16
17
18
19
20
21
22
23
24
25
26
27
28
29
30
31
32
33
34
35
36
37
38
39
40
41
42
43
44
45
46
47
48
49
50
51
52
53
54
55
56
57
58
59
60
EuN-like for high fluences might seem contradicting to the optical data showing similar
spectral shapes for all samples. This discrepancy shows once more that only a small
fraction of Eu is optically active while in EXAFS we probe the majority sites. This
interpretation is consistent with the slow increase/saturation of Eu-luminescence
intensity in NWs and the decrease in thin films (see Fig. 9).

CONCLUSIONS

GaN NWs and thin films were implanted with Eu ions in a fluence range from
 1×10^{13} at/cm² to 5×10^{15} at/cm². The distribution of Eu inside the NWs can be tuned by
adapting the NW diameter, density and implantation conditions as shown by Monte
Carlo simulations. Implantation damage was assessed by XRD revealing considerably
lower strain introduced by implantation defects in NWs than in thin films implanted in
the same condition. In good agreement, and despite a high level of surface defects, the
NW core is shown to be of high crystal quality for fluences as high as 1×10^{15} at/cm² and
after annealing. The formation of extended defects and defect clusters is suppressed
compared with implantation studies in GaN thin films. Optical activation of Eu^{3+} is
achieved upon annealing with similar optical centers in NWs and thin films. For the case
of NWs the CL emission intensity increases within the entire fluence range, while it
saturates or even decreases at higher fluences for the case of thin films suggesting
stronger luminescence quenching due to implantation defects in thin films. Eu ions
coexist in 2+ and 3+ charge state although Eu^{2+} can be almost suppressed by optimizing
the implantation and annealing conditions. The local lattice environment of Eu is similar

1
2
3 in NWs and thin films, however, in both cases it is strongly distorted by implantation
4 defects and the oversized Eu ion. In particular, for high fluences, EXAFS only shows a
5 signal from the first neighbor shell and suggests that a large fraction of Eu resides in a
6 EuN like configuration. For lower fluences and more efficient annealing techniques,
7 EXAFS results are consistent with a substitution of Ga by Eu. This transition from an EuN
8 to a GaN:Eu_{Ga} like structure occurs at lower fluences for NWs than for thin films
9 suggesting that the EuN like structure forms more easily in NWs. The presented results
10 help to establish guidelines for the use of ion implantation as processing tool for GaN
11 nanostructures. In particular, and despite the successful optical activation of Eu in all
12 samples, high fluences should be avoided due to severe surface damage and the
13 formation of local EuN-like structures.
14
15
16
17
18
19
20
21
22
23
24
25
26
27
28
29
30
31
32
33
34
35
36
37
38
39
40
41
42
43
44
45
46
47
48
49
50
51
52
53
54
55
56
57
58
59
60

SUPPORTING INFORMATION

Details of the dynamic Monte Carlo simulation

Details on XAS analysis:

- Eu charge state in GaN and changes of the XANES signal with X-ray irradiation
- Eu charge state in Si, SiO₂ and Si₃N₄
- EXAFS signal analysis

ACKNOWLEDGEMENTS

This work has been supported by the bilateral collaboration program Pessoa and the project NASIB funded by FCT and FEDER (PTDC/CTM-CTM/28011/2017, LISBOA-01-0145-FEDER-028011). We acknowledge support by FCT Portugal, through the individual grants SFRH/BPD/111285/2015 (MP). ARC acknowledges the grant by Ramón y Cajal programs (under contract number RYC-2015-18047). The research leading to these results has received funding from the European Union Seventh Framework Programme under Grant Agreement 312483 - ESTEEM2 (Integrated Infrastructure Initiative–I3), the ITN project “Supporting Postgraduate Research with Internships in industry and Training Excellence (SPRITE)” and the infrastructure project “Research And Development with Ion Beams – Advancing Technology in Europe (RADIATE)”. We thank I.S. Roqan (KAUST, Saudi Arabia) for the MOCVD GaN reference layers, M. Boćkowski (Unipress, Poland) for the HTHP annealing of the thin film reference sample, I. Kieffer (FAME beamline, ESRF, France) and E. Salas-Colera (SPLINE beamline, ESRF, France) for their help in recording good quality XAFS spectra and ESRF for the allocated beamtime (MA-2151, 30-02-1067, MA-2964).

REFERENCES

- (1) O'Donnell, K. P. and Dierolf V. (eds.) *Rare-Earth doped III-nitrides for optoelectronic and spintronic applications*; Springer, Dordrecht, 2010.
- (2) Nishikawa, A.; Kawasaki, T.; Furukawa, N.; Terai, Y.; Fujiwara, Y. Room-temperature red emission from a p-type/europium-doped/n-type gallium nitride light-emitting diode under current injection, *Appl. Phys. Express* **2009**, *2*, 071004.
- (3) O'Donnell, K. P.; Auf der Maur, M.; Di Carlo, A.; Lorenz, K. It's not easy being green: Strategies for all-nitrides, all-colour solid state lighting, *Phys. Status Solidi RRL* **2012**, *6*, 49-52.
- (4) Steckl, A. J.; Heikenfeld, J. C.; Lee, Dong Seon; Garter, M. J.; Baker, C. C.; Wang, Yongqiang; Jones, R. Rare-Earth-Doped GaN: Growth, properties, and fabrication of electroluminescent devices, *IEEE J. Sel. Top. Quantum Electron* **2002**, *8*, 749-766.
- (5) Lozykowski, H. J.; Jadwiszczak, W. M.; Brown, I. Visible cathodoluminescence of GaN doped with Dy, Er, and Tm, *Appl. Phys. Lett.* **1999**, *74*, 1129-1131.
- (6) Alves, E.; Lorenz, K.; Vianden, R.; Boemare, C.; Soares, M. J.; Monteiro, T. Optical doping of nitrides by ion implantation, *Mod. Phys. Lett. B* **2001**, *15*, 1281-1287.
- (7) Xu, C.; Chun, J.; Chon, B.; Joo, T.; Kim, D. E. In situ fabrication and blue shifted red emission of GaN:Eu nanoneedles, *Nanotechnology* **2007**, *18*, 015703.
- (8) Rodrigues, J.; Leitão, M. F.; Carreira, J. F. C.; Ben Sedrine, N.; Santos, N. F.; Felizardo, M.; Auzelle, T.; Daudin, B.; Alves, E.; Neves, A. J. et al. Spectroscopic analysis of Eu³⁺ implanted and annealed GaN layers and nanowires, *J. Phys. Chem. C* **2015**, *119*, 17954–17964.
- (9) Sekiguchi, H.; Nishikawa, S.; Imanishi, T.; Ozaki, K.; Yamane, K.; Okada, H.; Kishino, K.; Wakahara, A. Structural and optical properties of Eu-doped GaN nanocolumns on (111) Si substrates grown by RF-plasma-assisted molecular beam epitaxy, *Jap. J. Appl. Phys.* **2016**, *55*, 05FG07.
- (10) Consonni, V. Self-induced growth of GaN nanowires by molecular beam epitaxy: A critical review of the formation mechanisms, *Phys. Status Solidi RRL* **2013**, *7*, 699-712.
- (11) Aravindh, S. A.; and Roqan, I. S. Defect-impurity complex induced long-range ferromagnetism in GaN nanowires, *Mater. Res. Express* **2015**, *2*, 126104.
- (12) Woodward, N.; Nishikawa, A.; Fujiwara, Y.; Dierolf, V. Site and sample dependent electron–phonon coupling of Eu ions in epitaxial-grown GaN layers, *Opt. Mat.* **2011**, *33*, 1050–1054.
- (13) Bodiou, L.; Braud, A.; Doualan, J.-L.; Moncorgé, R.; Park, J. H.; Munasinghe, C.; Steckl, A. J.; Lorenz, K.; Alves, E.; Daudin, B. Optically active centers in Eu implanted, Eu in situ doped GaN, and Eu doped GaN quantum dots, *J. Appl. Phys.* **2009**, *105*, 043104.

- 1
2
3
4
5 (14) Rodrigues, J.; Ben Sedrine, N.; Felizardo, M.; Soares, M. J.; Alves, E.; Neves, A. J.;
6 Fellmann, V.; Tourbot, G.; Auzelle, T.; Daudin, B. et al. GaN:Pr³⁺ nanostructures for red solid
7 state light emission, *RSC Adv.* **2014**, *4*, 62869.
8
9 (15) Ronning, C.; Borschel, C.; Geburt, S.; Niepelt, R. Ion beam doping of semiconductor
10 nanowires, *Mater. Sci. Eng. R* **2010**, *70*, 30-43.
11
12 (16) Fukata, N.; Takiguchi, R.; Ishida, S.; Yokono, S.; Hishita, S.; Murakami, K.
13 Recrystallization and reactivation of dopant atoms in ion-implanted silicon nanowires, *ACS*
14 *Nano*, **2012**, *6*, 3278–3283.
15
16 (17) Kucheyev, S. O.; Williams, J.S.; Pearton, S. J. Ion implantation into GaN, *Mater. Sci. Eng.*
17 **2001**, *33*, 51-107.
18
19 (18) Lorenz, K.; Peres, M.; Franco, N.; Marques, J. G.; Miranda, S. M. C.; Magalhães, S.;
20 Monteiro, T.; Wesch, W.; Alves, E.; Wendler, E. Radiation damage formation and annealing in
21 GaN and ZnO, *Proc. of SPIE* **2011**, *7940*, 79400O.
22
23 (19) Ruterana, P.; Lacroix, B.; Lorenz, K. A Mechanism for damage formation in GaN during
24 rare earth ion implantation at medium range energy and room temperature, *J. Appl. Phys.* **2011**,
25 *109*, 013506.
26
27 (20) Turos, A. On the mechanism of damage buildup in gallium nitride, *Radiat. Eff. Defects*
28 **2013**, *168*, 431-441.
29
30 (21) Dhara, S.; Datta, A.; Wu, C. T.; Lan, Z. H.; Chen, K. H.; Wang, Y. L.; Chen, L. C.; Hsu, C.
31 W.; Lin, H. M.; Chen, C. C. Enhanced dynamic annealing in Ga⁺ ion-implanted GaN nanowires,
32 *Appl. Phys. Lett.* **2003**, *82*, 451-453.
33
34 (22) Dhara, S.; Datta, A.; Wu, C. T.; Chen, K. H.; Wang, Y. L.; Muto, S.; Tanabe, T.; Shen, C.
35 H.; Hsu, C. W.; Chen, L. C.; Maruyama, T. Mechanism of nanoblisters formation in Ga⁺ self-ion
36 implanted GaN nanowires, *Appl. Phys. Lett.* **2005**, *86*, 203119.
37
38 (23) Lorenz, K.; Nogales, E.; Miranda, S. M. C.; Franco, N.; Méndez, B.; Alves, E.; Tourbot,
39 G.; Daudin, B. Enhanced red emission from praseodymium doped GaN nanowires by defect
40 engineering, *Acta Materialia* **2013**, *61*, 3278–3284.
41
42 (24) Ullah, M. W.; Kuronen, A.; Stukowski, A.; Djurabekova, F.; Nordlund, K. Atomistic
43 simulation of Er irradiation induced defects in GaN nanowires. *J. Appl. Phys.* **2014**, *116*,
44 124313.
45
46 (25) Bartels, J.; Freitag, K.; Marques, J. G.; Soares, J. C.; Vianden, R. Incorporation of the
47 transition metal Hf into GaN, *Hyp. Int.* **1999**, *120-121*, 397-402.
48
49 (26) Lorenz, K.; Wahl, U.; Alves, E.; Nogales, E.; Dalmaso, S.; Martin, R. W.; O'Donnell, K.
50 P.; Wojdak, M.; Braud, A.; Monteiro, T. et al. High temperature annealing of rare earth
51 implanted GaN films: Structural and optical properties, *Opt. Mater.* **2006**, *28*, 750-758.
52
53
54
55
56
57
58
59
60

- (27) Roqan, I. S.; O'Donnell, K. P.; Martin, R. W.; Edwards, P. R.; Song, S. F.; Vantomme, A.; Lorenz, K.; Alves, E.; Boćkowski, M. Identification of the prime optical center in GaN:Eu³⁺, *Phys. Rev. B* **2010**, *81*, 085209.
- (28) Auzelle, T.; Haas, B.; Minj, A.; Bougerol, C.; Rouvière, J.-L.; Cros, A.; Colchero, J.; Daudin, B. The influence of AlN buffer over the polarity and the nucleation of self-organized GaN nanowires, *J. Appl. Phys.* **2015**, *117*, 245303.
- (29) Möller, W. TRI3DYN – Collisional computer simulation of the dynamic evolution of 3-dimensional nanostructures under ion irradiation, *Nucl. Instr. and Meth. Phys. Res. B* **2014**, *322*, 23–33.
- (30) Möller, W.; Johannes, A.; Ronning, C. Shaping and compositional modification of zinc oxide nanowires under energetic manganese ion irradiation, *Nanotechnology* **2016**, *27*, 175301.
- (31) Berencén, Y.; Prucnal, S.; Möller, W.; Hübner, R.; Rebohle, L.; Böttger, R.; Glaser, M.; Schönherr, T.; Yuan, Y.; Wang, M.; Georgiev, Y.M.; Erbe, A.; Lugstein, A.; Helm, M.; Zhou, S.; Skorupa, W. CMOS-Compatible Controlled Hyperdoping of Silicon Nanowires, *Adv. Mater. Interfaces* **2018**, 1800101.
- (32) Lorenz, K.; Miranda, S. M. C.; Alves, E.; Roqan, I. S.; O'Donnell, K. P.; Boćkowski, M. High pressure annealing of Europium implanted GaN, *Proc. of SPIE* **2012**, *8262*, 82620C.
- (33) Drouin, D.; Couture, A. R.; Joly, D.; Tastet, X.; Aimez, V.; Gauvin, R. CASINO V2.42: a fast and easy-to-use modeling tool for scanning electron microscopy and microanalysis users, *Scanning* **2007**, *29*, 92.
- (34) Zagonel, L. F.; Mazzucco, S.; Tencé, M.; March, K.; Bernard, R.; Laslier, B.; Jacopin, G.; Tchernycheva, M.; Rigutti, L.; Julien, F. H.; Songmuang, R.; Kociak, M. Nanometer scale spectral imaging of quantum emitters in nanowires and its correlation to their atomically resolved structure, *Nano Lett.* **2011**, *11*, 568–573.
- (35) Proux, O.; Nassif, V.; Prat, A.; Ulrich, O.; Lahera, E.; Biquard, X.; Menthonnex, J.-J.; Hazemann, J.-L. Feedback system of a liquid nitrogen cooled double-crystal monochromator: design and performances, *J. Synchrotron Radiation* **2006**, *13*, 59-68.
- (36) Proux, O.; Biquard, X.; Lahera, E.; Menthonnex, J.-J.; Prat, A.; Ulrich, O.; Soldo, Y.; Trévisson, P.; Kapoujvan, G.; Perroux, G. et al. FAME: A new beamline for X-ray absorption investigations of very-diluted systems of environmental, material and biological interests, *Physica Scripta* **2005**, *115*, 970-973.
- (37) Rubio-Zuazo, J.; Collado-Negro, V.; Heyman, C.; Ferrer, P.; da Silva, I.; Gallastegui, J. A.; Gutiérrez-León A.; Castro, G.R. A double crystal X-ray monochromator for the SpLine diffraction and absorption synchrotron bending magnet beamline at the ESRF, *J. Phys.: Conf. Series* **2013**, *425*, 052005.

- (38) Ravel B. and Newville, M. ATHENA, ARTEMIS, HEPHAESTUS: data analysis for X-ray absorption spectroscopy using IFEFFIT, *J. Synchrotron Radiation* **2005**, *12*, 537–541.
- (39) Ren, W.; Kuronen, A.; Nordlund, K. Atomistic simulation of irradiation effects in GaN nanowires, *Nucl. Instr. Meth. Phys. Res. B* **2014**, *326*, 15–18.
- (40) Liu, C.; Mensching, B.; Volz, K.; Rauschenbach, B. Lattice expansion of Ca and Ar ion implanted GaN, *Appl. Phys. Lett.* **1997**, *71*, 2313-2315.
- (41) Lacroix, B.; Leclerc, S.; Declémy, A.; Lorenz, K.; Alves E.; Ruterana, P. Mechanisms of damage formation in Eu-implanted GaN probed by X-ray diffraction, *Europhysics Lett.* **2011**, *96*, 46002.
- (42) Pipeleers, B.; Hogg, S. M.; Vantomme, A. Influence of the implantation angle on the generation of defects for Er implanted GaN, *Nucl. Instr. Meth. Phys. Res. B* **2003**, *206*, 95-98.
- (43) Faye, D. Nd.; Wendler, E.; Felizardo, M.; Magalhães, S.; Alves, E.; Brunner, F.; Weyers, M.; Lorenz, K. Mechanisms of implantation damage formation in $\text{Al}_x\text{Ga}_{1-x}\text{N}$ compounds, *J. Phys. Chem. C* **2016**, *120*, 7277–7283.
- (44) Magalhães, S.; Fialho, M.; Peres, M.; Lorenz K.; Alves, E. Quantitative x-ray diffraction analysis of bimodal damage distributions in Tm implanted $\text{Al}_{0.15}\text{Ga}_{0.85}\text{N}$, *J. Phys. D: Appl. Phys.* **2016**, *49*, 135308.
- (45) Pagowska, K.; Ratajczak, R.; Stonert, A.; Turos, A.; Nowicki, L.; Sathish, N.; Józwick P.; Muecklich, A. RBS/Channeling and TEM study of damage buildup in ion bombarded GaN, *Acta Physica Polonica* **2011**, *120*, 153.
- (46) Kaganer, V. M.; Wölz, M.; Brandt, O.; Geelhaar, L.; Riechert, H. X-ray diffraction profiles from axial nanowire heterostructures, *Phys. Rev. B* **2011**, *83*, 245321.
- (47) Kaganer, V. M.; Jenichen, B.; Brandt, O.; Fernández-Garrido, S.; Dogan, P.; Geelhaar, L.; Riechert, H. Inhomogeneous strain in GaN nanowires determined from x-ray diffraction peak profiles, *Phys. Rev. B* **2012**, *86*, 115325.
- (48) Debelle, A.; Declémy, A. XRD investigation of the strain/stress state of ion-irradiated crystals, *Nucl. Instr. and Meth. Phys. Res. B* **2010**, *268*, 1460–1465.
- (49) Miranda, S. M. C.; Edwards, P. R.; O'Donnell, K. P.; Boćkowski, M.; Alves, E.; Roqan, I. S.; Vantomme, A.; Lorenz, K. Sequential multiple-step europium ion implantation and annealing of GaN, *Phys. Stat. Sol. C* **2014**, *11*, 253–257.
- (50) Lorenz, K.; Wendler, E.; Redondo-Cubero, A.; Catarino, N.; Chauvat, M.-P.; Schwaiger, S.; Scholz, F.; Alves, E.; Ruterana, P. Implantation damage formation in a-, c- and m-plane GaN, *Acta Materialia* **2017**, *123*, 177-187.
- (51) Potin, V.; Ruterana P.; Nouet, G. HREM study of stacking faults in GaN layers grown on sapphire substrate, *J. Phys. Condensed Matter* **2000**, *12*, 10301-10306.

- (52) Gloux, F.; Wojtowicz, T.; Ruterana, P.; Lorenz, K.; Alves, E. Transmission electron microscopy investigation of the structural damage formed in GaN by medium range energy rare earth ion implantation, *J. Appl. Phys.* **2006**, *100*, 073520.
- (53) Lorenz, K.; Barradas, N. P.; Alves, E.; Roqan, I. S.; Nogales, E.; Martin, R. W.; O'Donnell, K. P.; Gloux, F.; Ruterana, P. Structural and optical characterization of Eu-implanted GaN, *J. Phys. D: Appl. Phys.* **2009**, *42*, 165103.
- (54) Lorenz, K.; Alves, E.; Gloux, F.; Ruterana, P.; Peres, M.; Neves, A. J.; Monteiro, T. Optical doping and damage formation in AlN by Eu implantation, *J. Appl. Phys.* **2010**, *107*, 023525.
- (55) Lorenz, K.; Alves, E.; Roqan, I. S.; O'Donnell, K. P.; Nishikawa, A.; Fujiwara, Y.; Boćkowski, M. Lattice site location of optical centers in GaN:Eu light emitting diode material grown by organometallic vapor phase epitaxy, *Appl. Phys. Lett.* **2010**, *97*, 111911.
- (56) de Boer, W. D. A. M.; McGonigle, C.; Gregorkiewicz, T.; Fujiwara, Y.; Tanabe, S.; Stallinga, P. Optical excitation and external photoluminescence quantum efficiency of Eu³⁺ in GaN, *Scientific Reports* **2014**, *4*, 5235.
- (57) Lorenz, K.; Vianden, R.; Birkhahn, R.; Steckl, A. J.; da Silva, M. F.; Soares, J. C.; Alves, E. RBS/channeling study of Er doped GaN films grown by MBE on Si (111), *Nucl. Instr. Meth. Phys. Res. B* **2000**, *161-163*, 946-951.
- (58) Wahl, U.; Alves, E.; Lorenz, K.; Monteiro, T.; Vantomme, A.; de Vries, B.; Vianden, R. Lattice location and optical activation of rare earth implanted GaN, *Mater. Sci. Eng. B* **2003**, *105*, 132-140.
- (59) Filhol, J. S.; Jones, R.; Shaw, M. J.; Briddon, P. R. Structure and electrical activity of rare-earth dopants in GaN, *Appl. Phys. Lett.* **2004**, *84*, 2841.
- (60) Sanna, S.; Schmidt, W. G.; Frauenheim, Th.; Gerstmann, U. Rare-earth defect pairs in GaN: LDA+U calculations, *Phys. Rev. B* **2009**, *80*, 104120.
- (61) Ofuchi, H.; Nishiwaki, T.; Takaba, K.; Ogawa, K.; Tabuchi, M.; Takeda, Y.; Wakahara, A.; Yoshida, A.; Ohshima, T.; Ito, H. Fluorescence EXAFS study on local structures around Eu atoms implanted in Al_xGa_{1-x}N, *Physica B* **2006**, *376-377*, 496-498.
- (62) Ofuchi, H.; Honma, T.; Kawasaki, T.; Furukawa, N.; Nishikawa, A.; Fujiwara, Y. Fluorescence XAFS analysis of Eu-doped GaN layers grown by organometallic vapor phase epitaxy, *e-J. Surf. Sci. Nanotech.* **2011**, *9*, 51-53.
- (63) Lupan, O.; Pauporté, T.; Viana, B.; Aschehoug, P.; Ahmadi, M.; Roldan Cuenya, B.; Rudzevich, Y.; Lin, Y.; Chow, L. Eu-doped ZnO nanowire arrays grown by electrodeposition, *Appl. Surface Science* **2013**, *282*, 782-788.
- (64) Geburt, S.; Lorke, M.; da Rosa, A. L.; Frauenheim, T.; Röder, R.; Voss, T.; Kaiser, U.; Heimbrodt, W.; Ronning, C. Intense intrashell luminescence of Eu-doped single ZnO

1
2
3
4
5 nanowires at room temperature by implantation created Eu–O_i complexes, *Nano Lett.* 2014, 14,
6 4523–4528.

7
8 (65) Lorke, M.; Frauenheim, T.; da Rosa, A. L. Many-body electronic structure calculations of
9 Eu-doped ZnO, *Phys. Rev. B* **2016**, 93, 115132.

10
11 (66) Shannon, R. D. Revised effective ionic radii and systematic studies of interatomic
12 distances in halides and chalcogenides, *Acta Cryst. A* **1976**, 32, 751-767.

13
14 (67) Katchkanov, V.; Mosselmans, J. F. W.; O'Donnell, K. P.; Nogales, E.; Hernandez, S.;
15 Martin, R. W.; Steckl, A.; Lee, D. S. Extended X-ray absorption fine structure studies of GaN
16 epilayers doped with Er, *Opt. Mater.* **2006**, 28, 785–789.

17
18 (68) Katsikini, M.; Kachkanov, V.; Boulet, P.; Edwards, P. R.; O'Donnell, K. P.; Brien, V.
19 Extended X-ray absorption fine structure study of the Er bonding in AlNO:Er_x films with x ≤
20 3.6%, *J. Appl. Phys.* **2018**, 124, 085705.

21
22 (69) Wyckoff, R. W. G. Second edition, Interscience Publishers, New York, *Crystal Structures*,
23 **1963**, 1, 85-237.

FIGURES

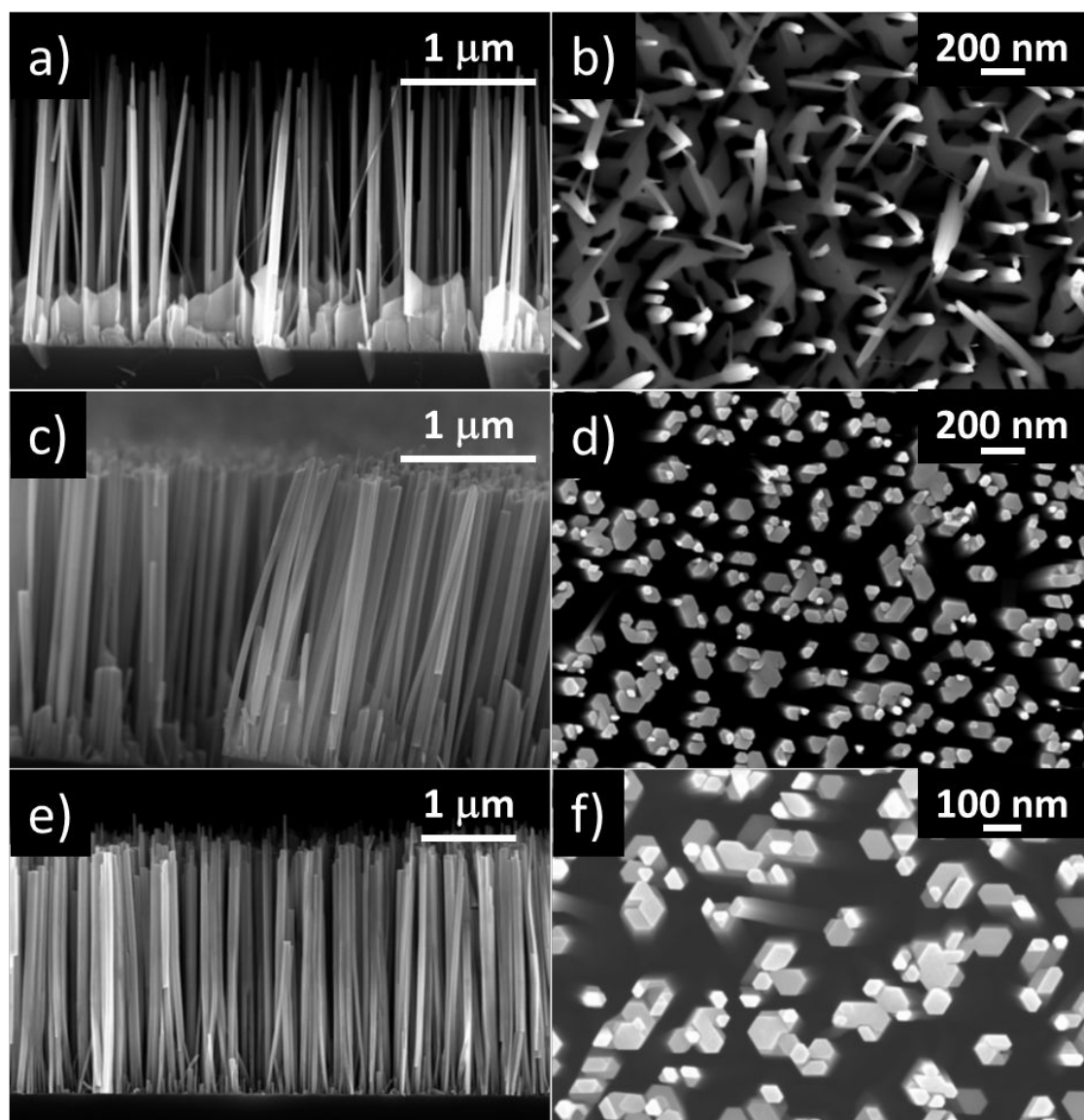


Fig. 1: SEM side-view and top view images of the nanowires used for XRD, TEM and CL analysis (set 1) corresponding to the wafer centre (a and b) and to the wafer periphery (c and d). e) and f) show typical SEM images of the NWs used for XANES and EXAFS analysis (set 2).

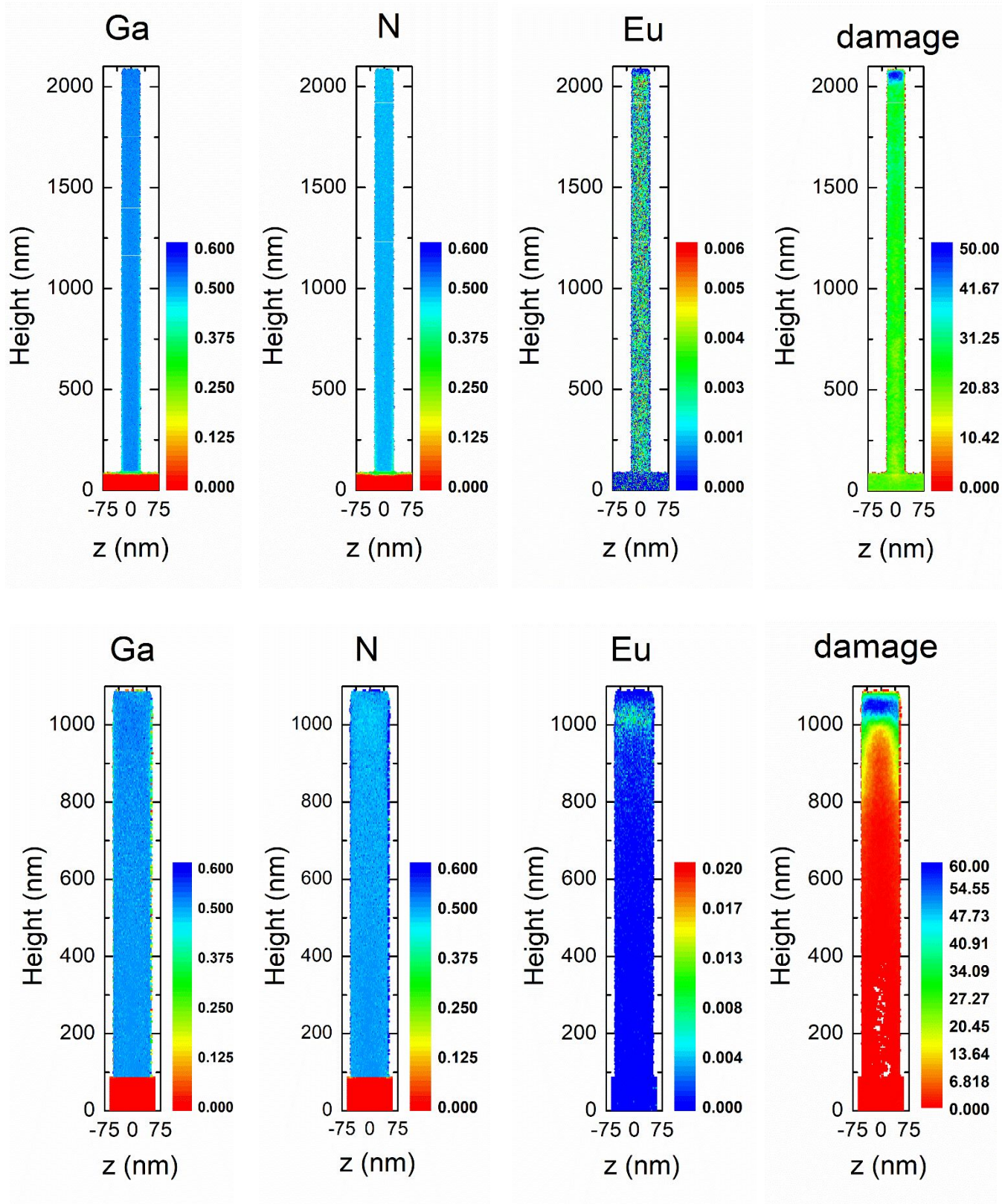


Fig. 2: TRI3DYN simulation results showing the elemental distribution of Ga, N and Eu as well as the damage distribution (in dpa) in a longitudinal slice of 8 nm thickness along

1
2
3 the NW length. Top: for an array of 50 nm diameter NWs with an areal density of 2×10^9
4 cm^{-2} ; Bottom: for an array of 100 nm diameter and an areal density of $7 \times 10^9 \text{ cm}^{-2}$.
5
6
7
8
9
10
11
12
13
14
15
16
17
18
19
20
21
22
23
24
25
26
27
28
29
30
31
32
33
34
35
36
37
38
39
40
41
42
43
44
45
46
47
48
49
50
51
52
53
54
55
56
57
58
59
60

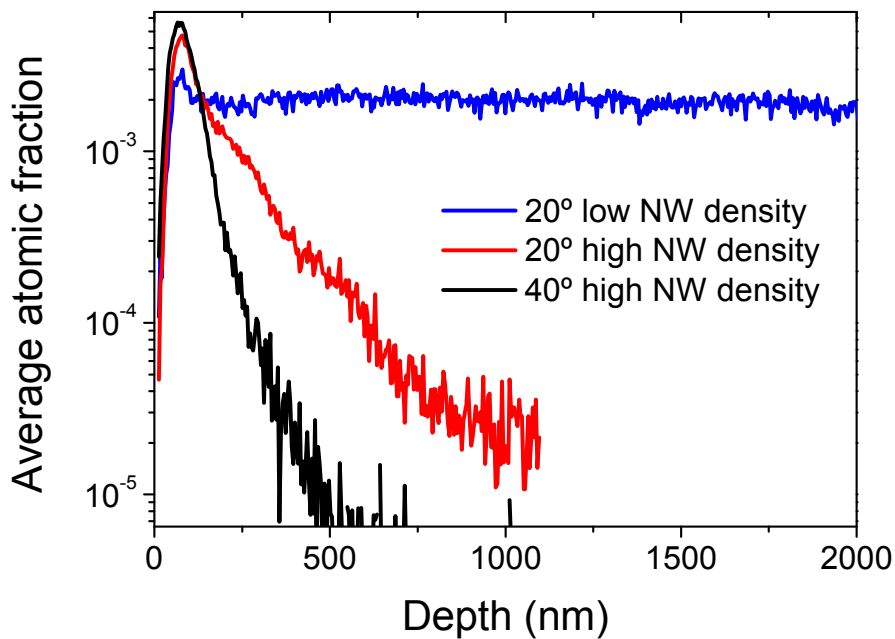


Fig. 3: TRI3DYN simulation results showing the average atomic Eu fraction along the NW length for the three combinations of implantation angle, NW diameter and density.

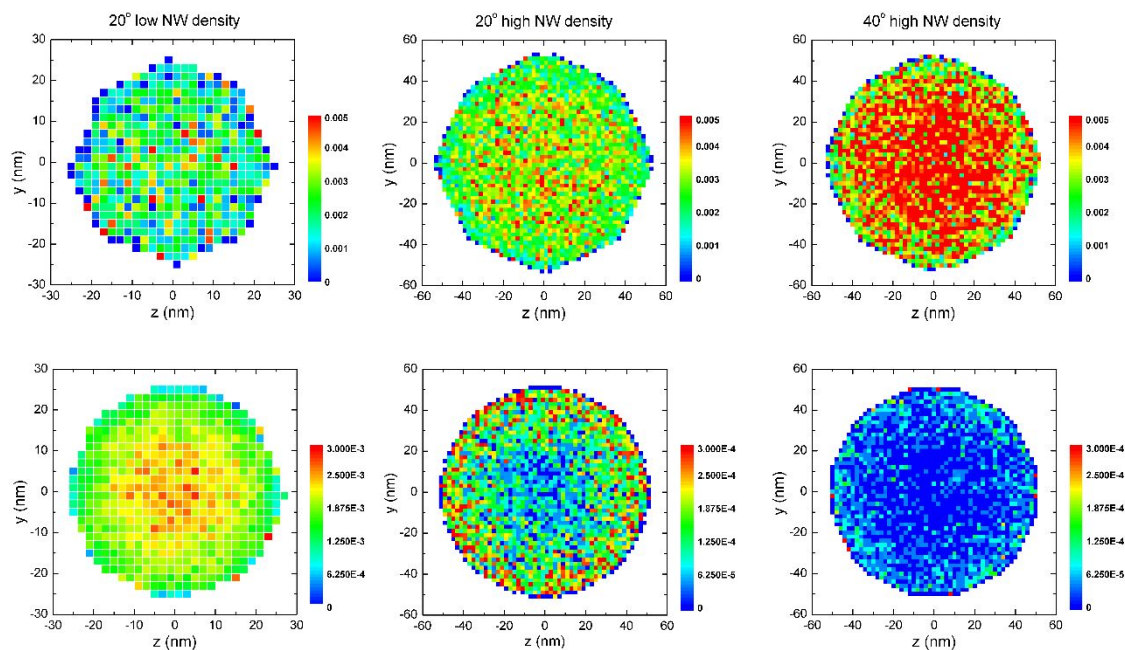


Fig. 4: TRI3DYN simulation results showing the lateral distribution of Eu for the three combinations of implantation angle, NW diameter and density. Top: The data was integrated close to the tip of the NW corresponding to the end of range of ions entering the NW from the top. Bottom: The data was integrated from ~ 50 -150 depth until the NW base in order to disregard ions that entered the NWs from the top surface.

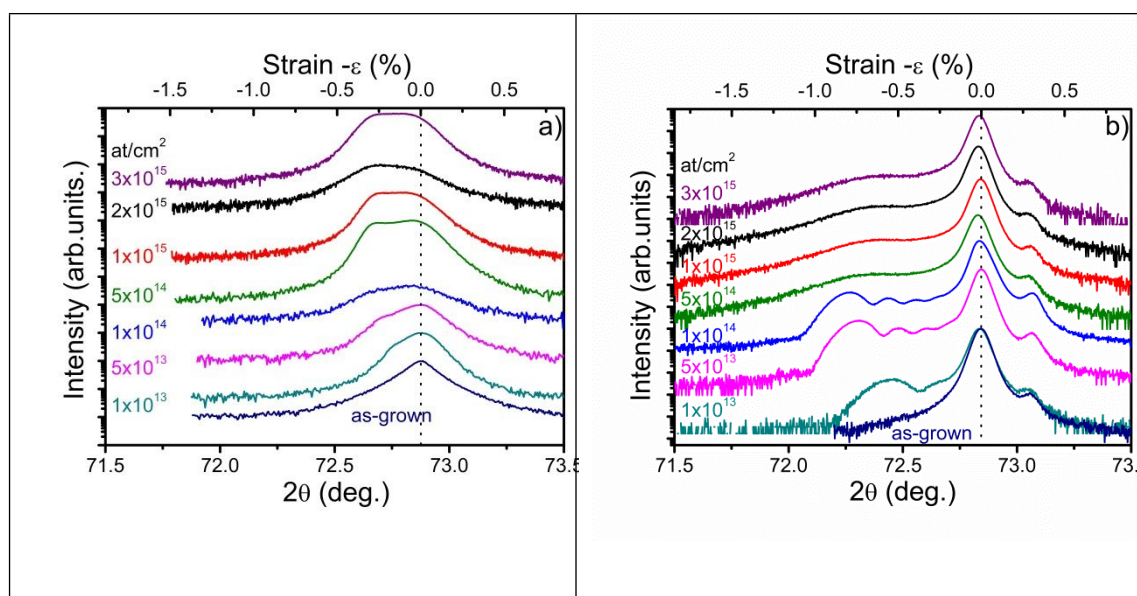


Fig. 5: XRD (0004) 2θ - θ curves for the first set of NWs (a) and reference thin films (b) implanted to different fluences at 20° incidence. Note that the small peak at $\sim 73.1^\circ$ visible in b) is an artefact of the XRD system due to the incomplete suppression of the $\text{CuK}_{\alpha 2}$ line.

1
2
3
4
5
6
7
8
9
10
11
12
13
14
15
16
17
18
19
20
21
22
23
24
25
26
27
28
29
30
31
32
33
34
35
36
37
38
39
40
41
42
43
44
45
46
47
48
49
50
51
52
53
54
55
56
57
58
59
60

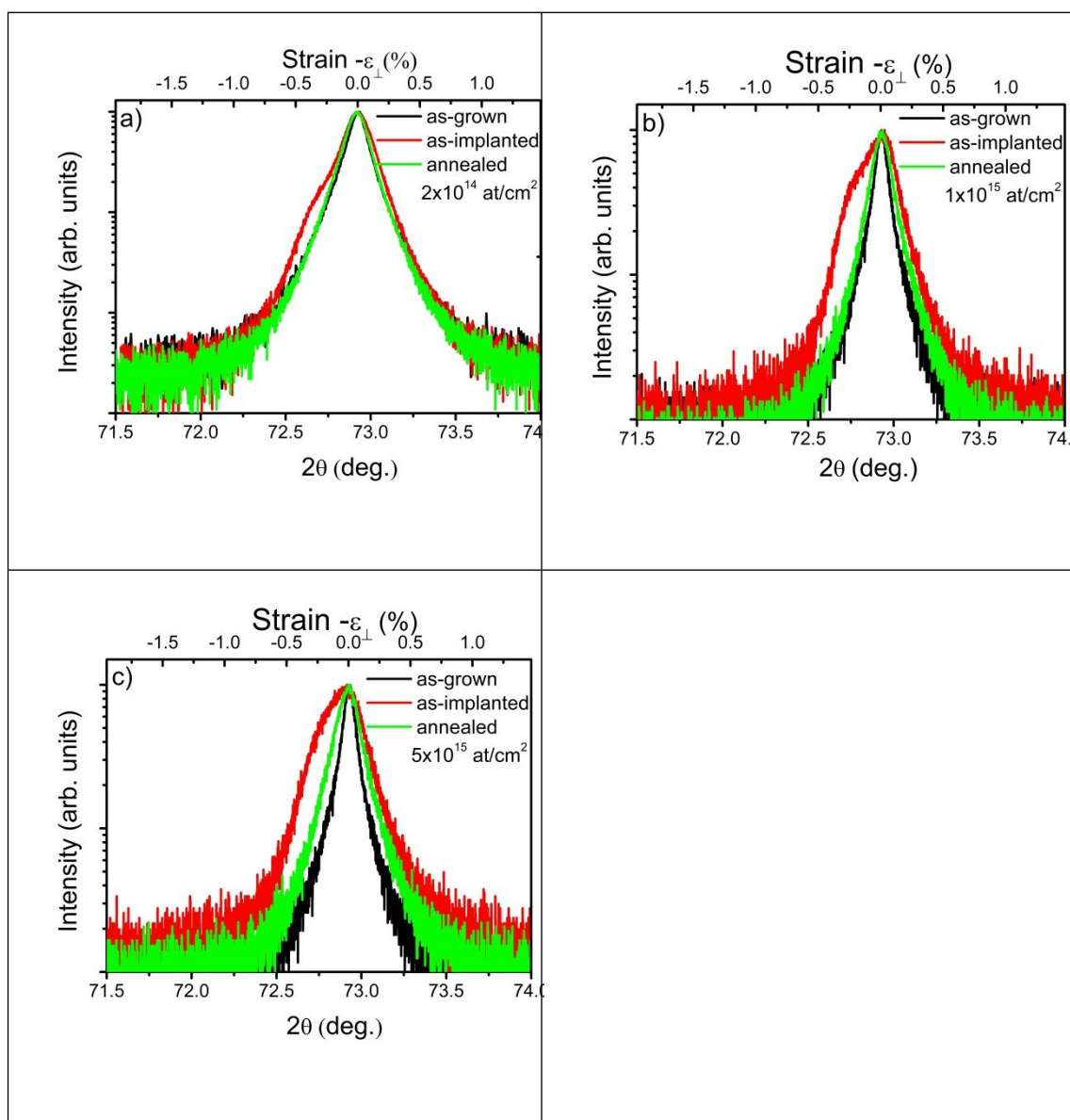


Fig. 6: XRD 2θ - θ curves of high density GaN NWs implanted with 40° tilt comparing as-grown, as-implanted and annealed samples implanted to fluences of 2×10^{14} at/cm 2 (a) 1×10^{15} at/cm 2 (b) and 5×10^{15} at/cm 2 (c).

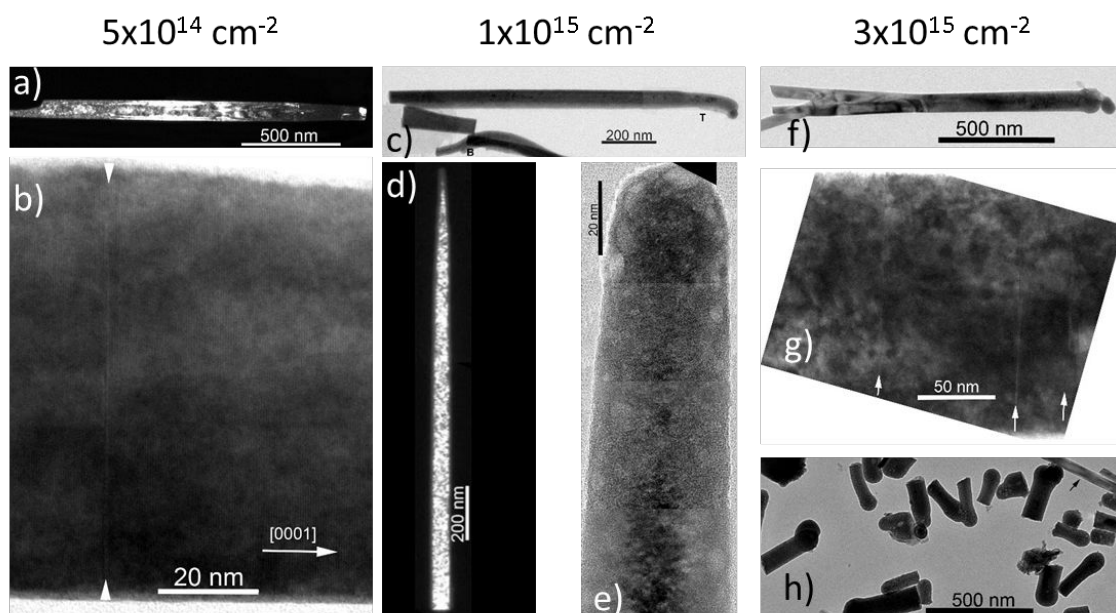


Fig. 7: TEM images of as-implanted NWs implanted to a fluence of $5 \times 10^{14} \text{ cm}^{-2}$ (a,b), $1 \times 10^{15} \text{ cm}^{-2}$ (c-e) and $3 \times 10^{15} \text{ cm}^{-2}$ (f-h). Basal stacking faults are marked by white arrows.

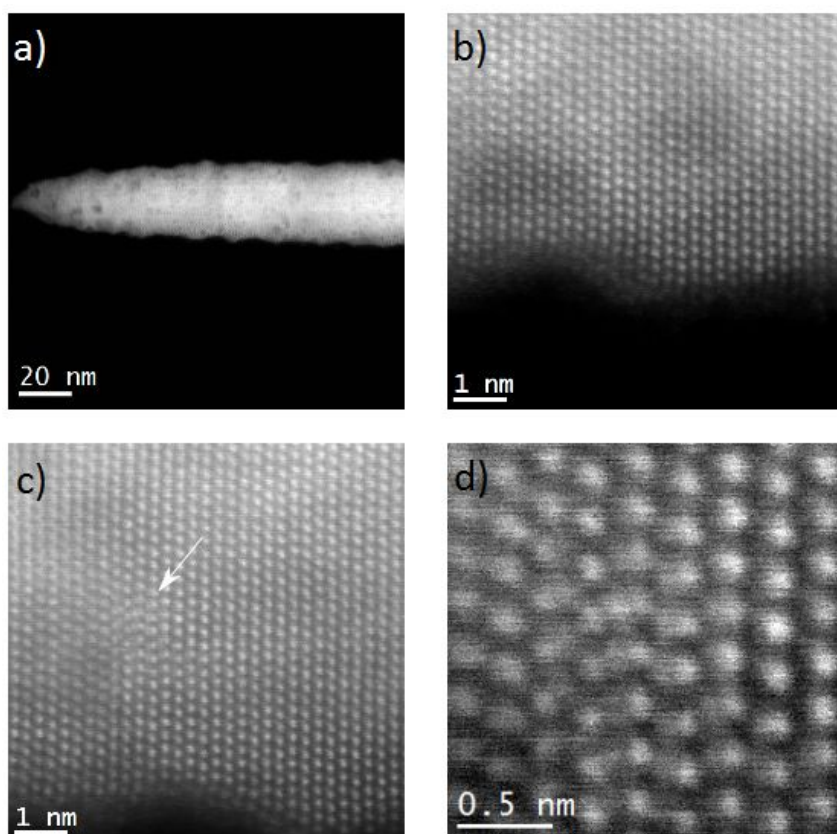


Fig. 8: a) STEM HAADF image of a NW implanted to a fluence of 1×10^{15} at/cm² and annealed at 1000 °C. b) - d) High resolution STEM HAADF images of the same NW showing high crystalline quality of the NW core (b) and an isolated extended defect (c and d).

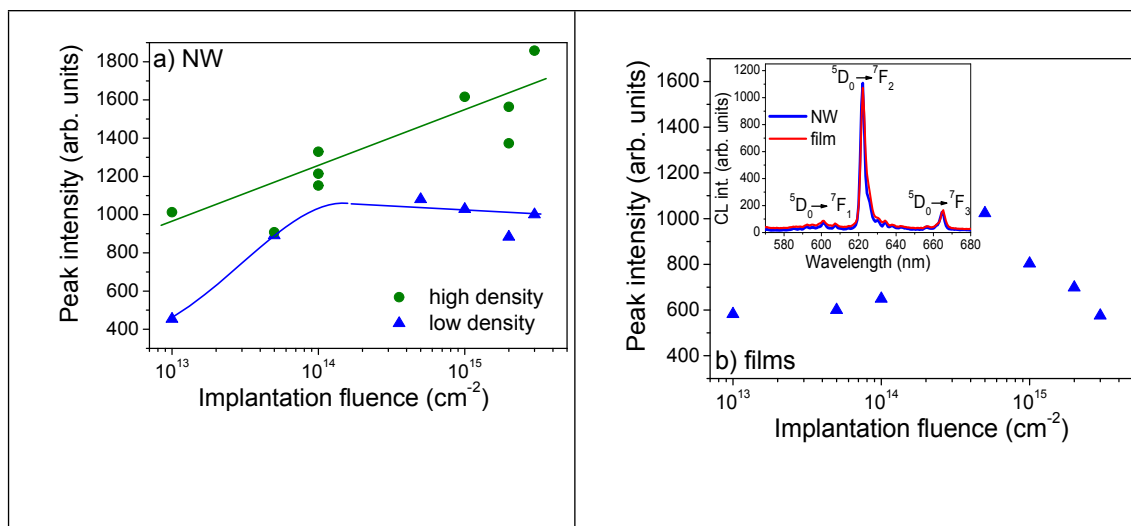


Fig. 9: RT CL peak intensity of the Eu³⁺ emission line at ~622 nm as a function of the fluence for NWs in regions with low and high NW density (a) and thin film reference samples (b). The inset in b) compares typical CL spectra for NW and thin film samples.

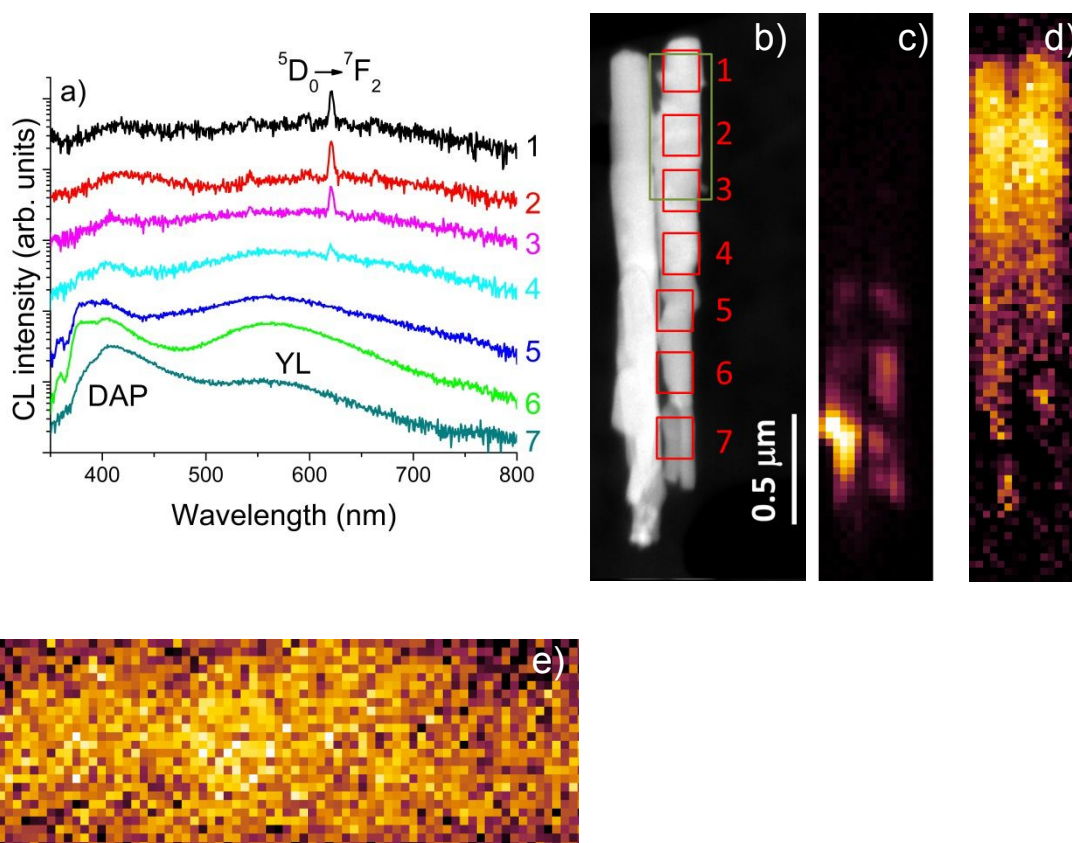


Fig. 10: a) Nano-CL spectra taken at seven points from the top (1) to the bottom (7) of a single NW implanted to a fluence of 1×10^{14} at/cm² (20° incidence angle) and annealed at 1000 °C. The regions at which the spectra were taken are indicated with red rectangles in (b). (c) and (d) Luminescence intensity maps integrating the spectra in a wavelength region from 350 to 550 nm (c) and around the 622 nm Eu³⁺ line (d). (e) Detail of the luminescence intensity map integrating the Eu³⁺ emission peak at 622 nm in the region with highest Eu-emission marked with the bigger green rectangle in b); the pixel size is 10×10 nm².

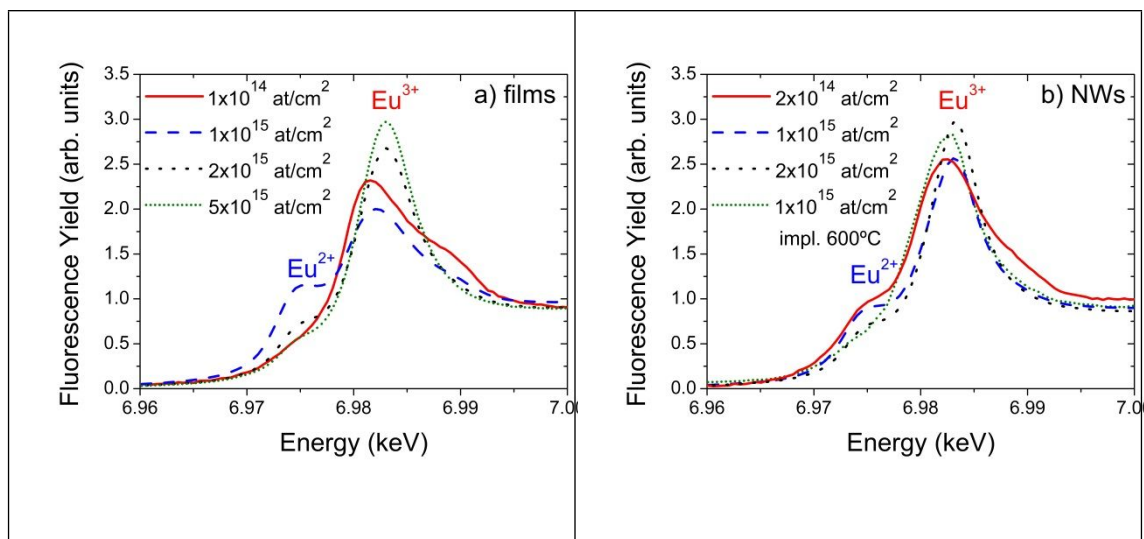


Fig. 11: XANES spectra for selected thin films (a) and NWs (b) showing the coexistence of Eu in the 2+ and 3+ charge state and the possibility of decreasing the Eu²⁺ fraction by HTHP annealing or implantation at elevated temperature plus RTA at 1000 °C. The Eu²⁺ edge is found at a fixed position in all samples while the position of the Eu³⁺ varies slightly for different implantation/annealing conditions.

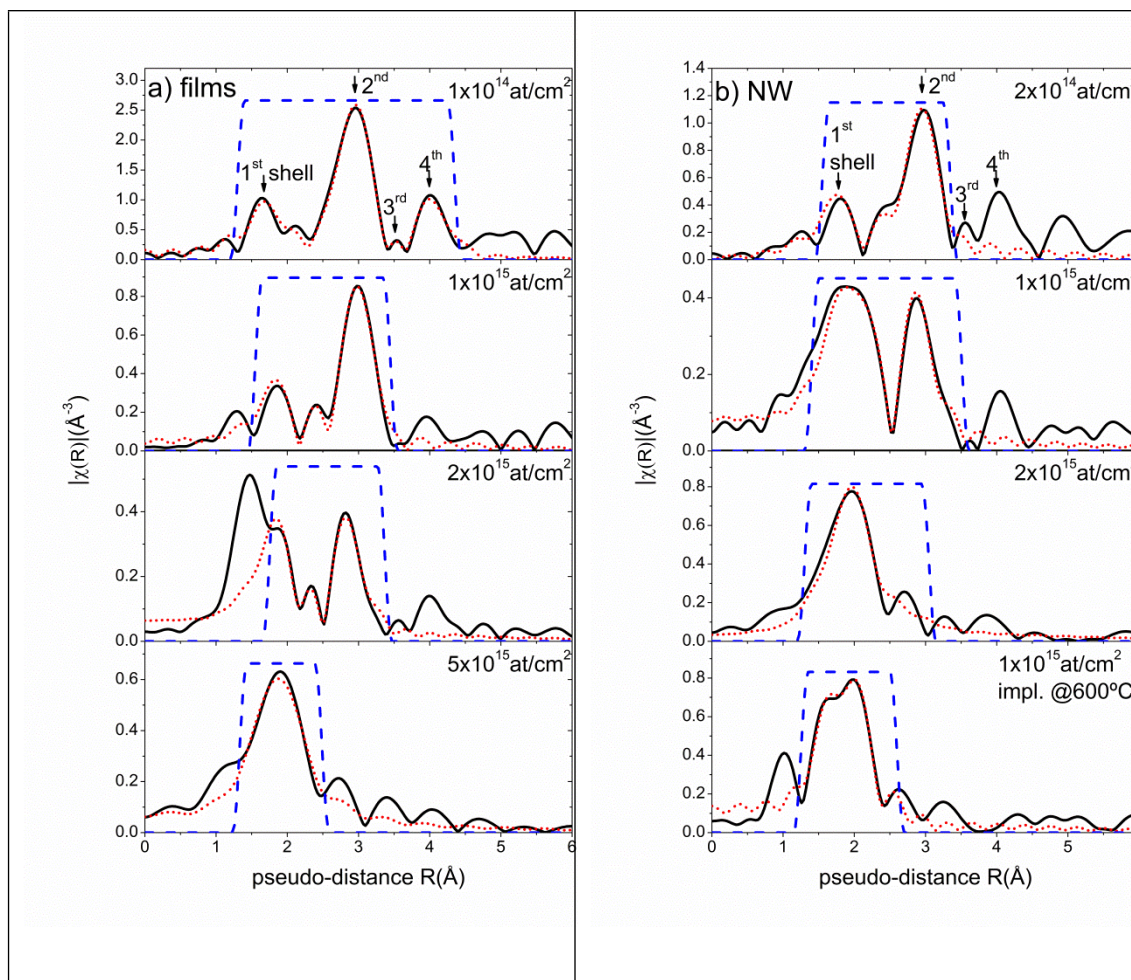


Fig. 12: Fourier transform of the EXAFS signal and fits of selected films (a) and NWs (b) showing the experimental data (black solid line), the fit (red dotted line) and the window used to do the fit (blue dashed line). Note that in thin film sample $2 \times 10^{15} \text{ at/cm}^2$, the low-R bump is an artefact arising from a baseline residual oscillation that could not be suppressed.

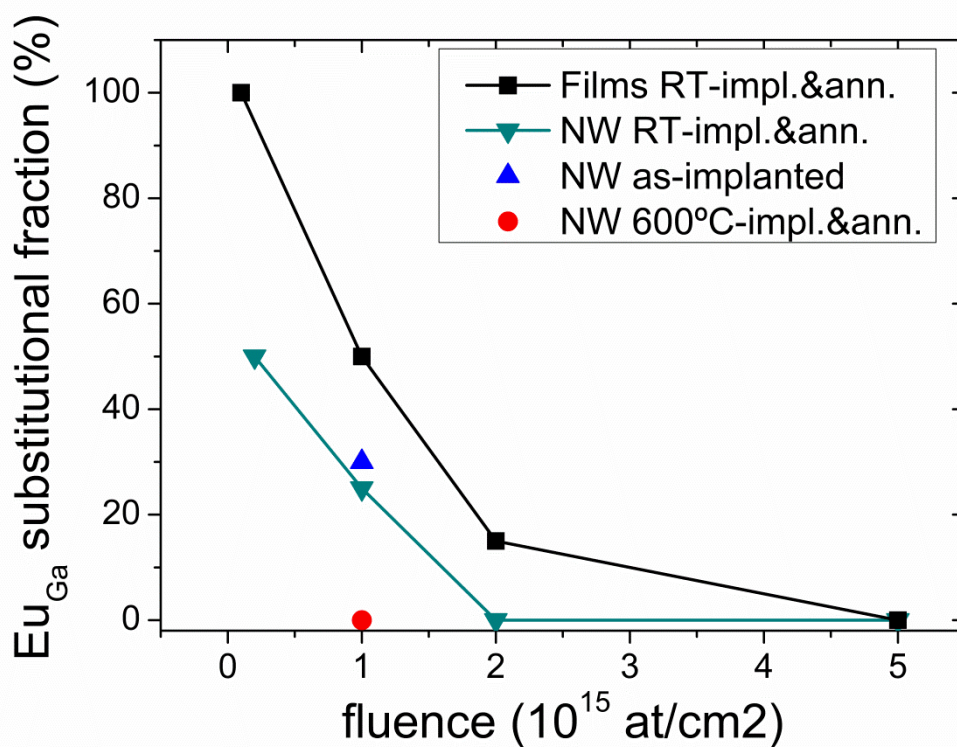
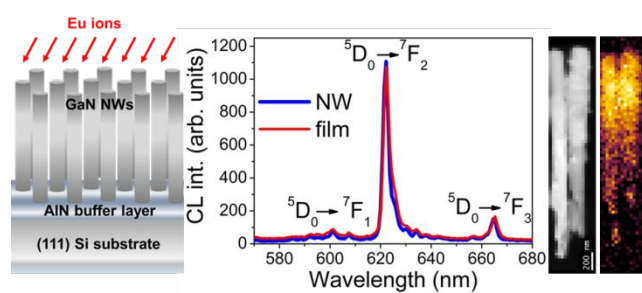
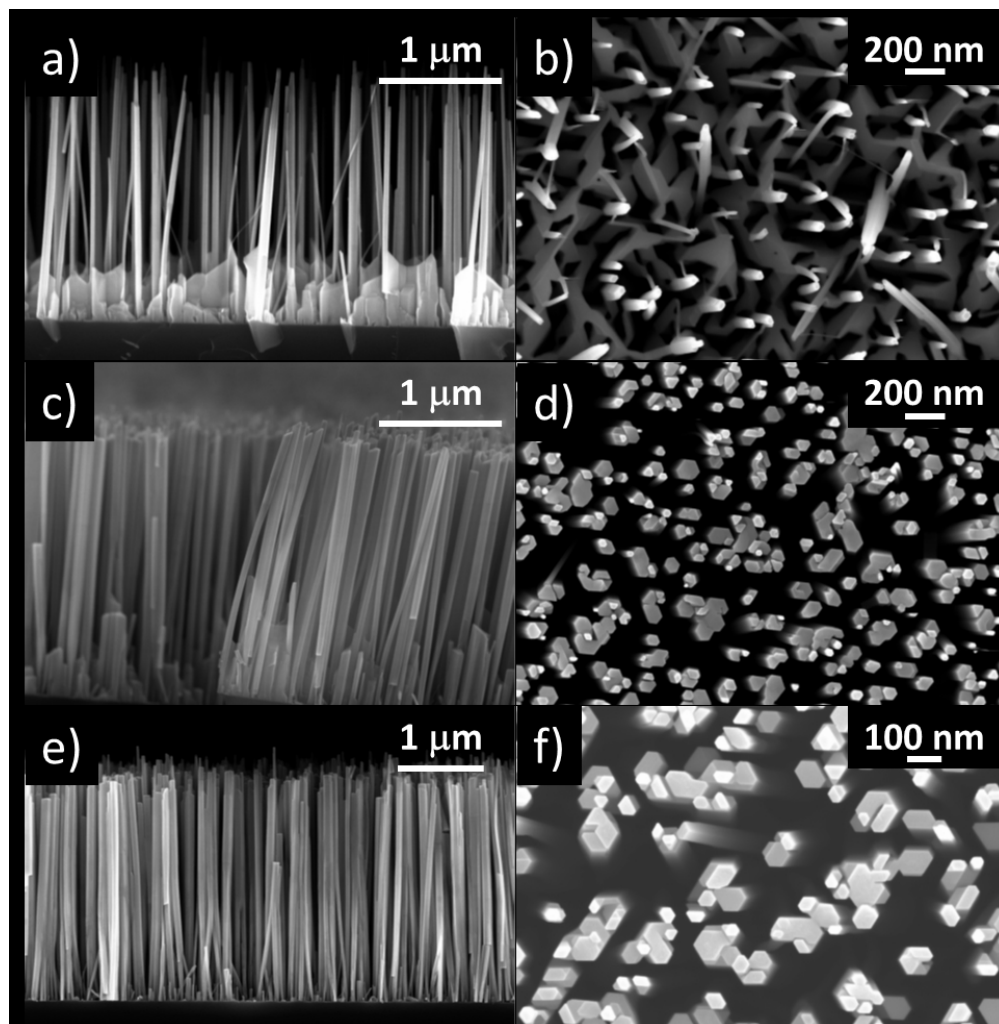


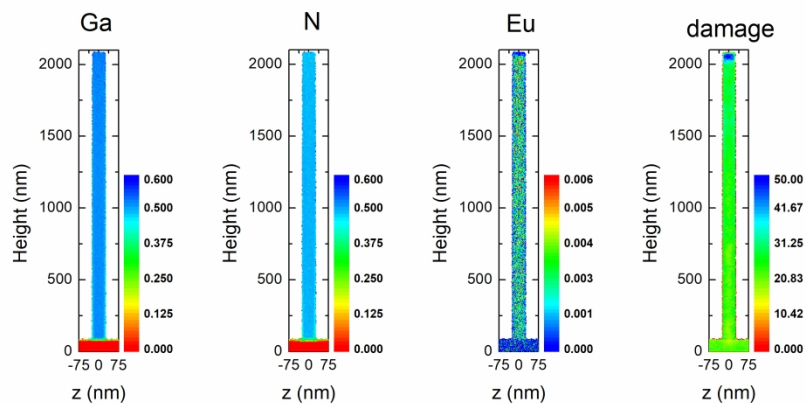
Fig. 13: Fraction of Eu incorporated in substitutional Ga-sites as a function of the fluence for thin film and NW samples in different conditions as given in the legend. RT-impl.: implanted at RT; 600 °C-impl.: implanted at 600 °C; ann: annealed at 1000 °C except for the thin film sample implanted to 1×10^{14} at/cm² which was annealed at 1400 °C.

TOC graphic:

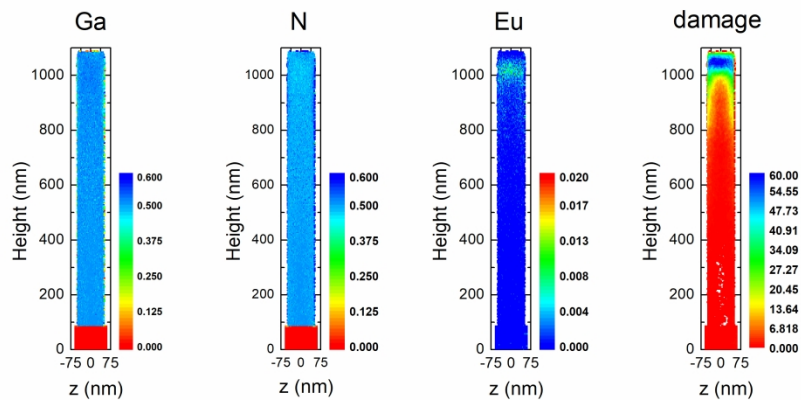




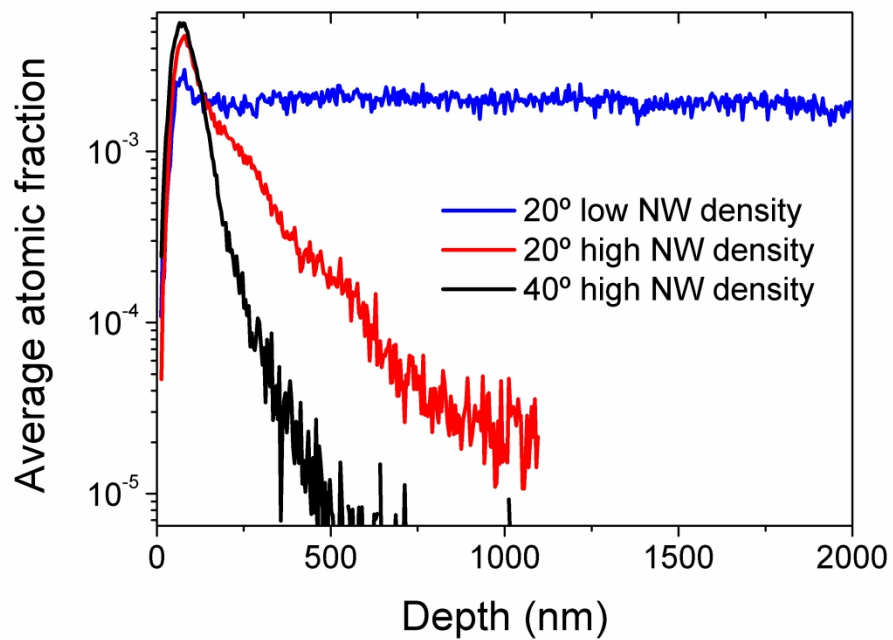
162x165mm (150 x 150 DPI)



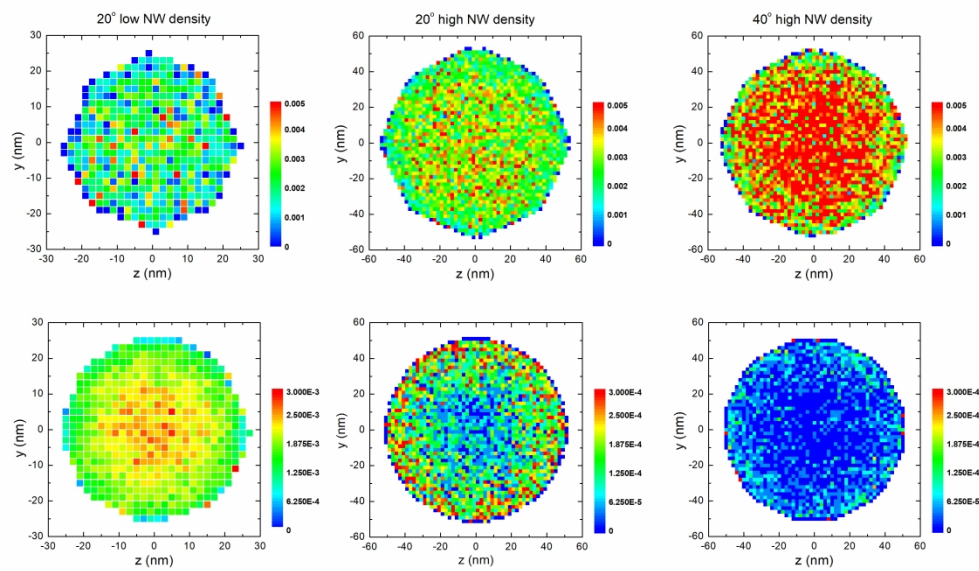
287x202mm (300 x 300 DPI)



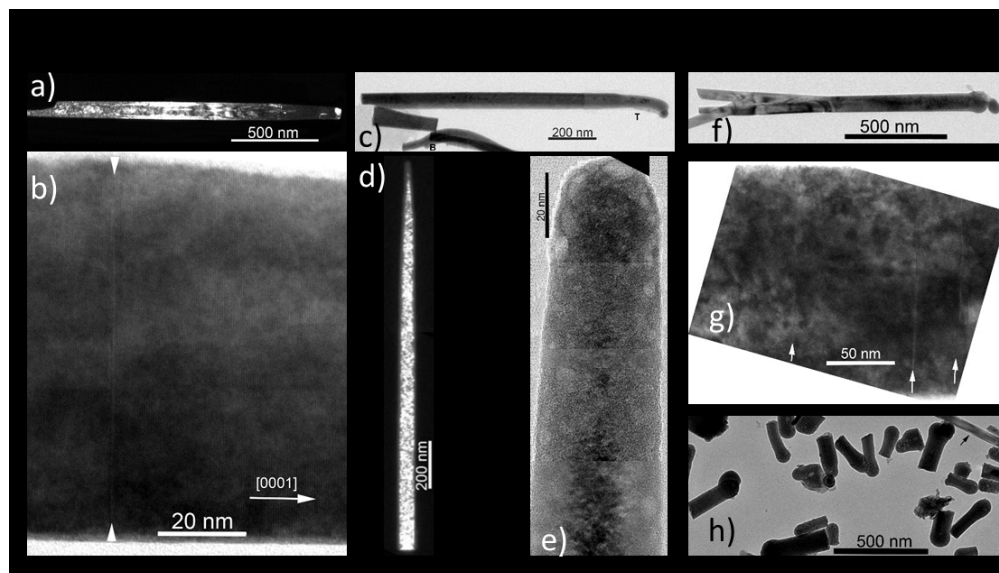
287x202mm (300 x 300 DPI)



282x220mm (300 x 300 DPI)

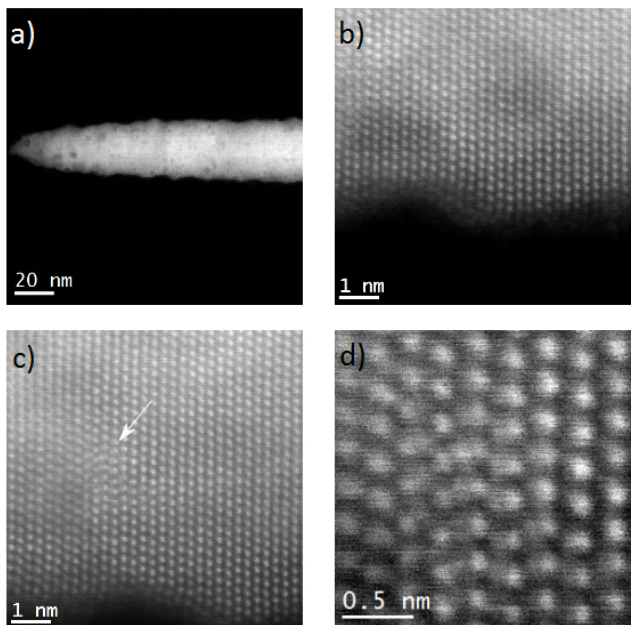


287x203mm (300 x 300 DPI)

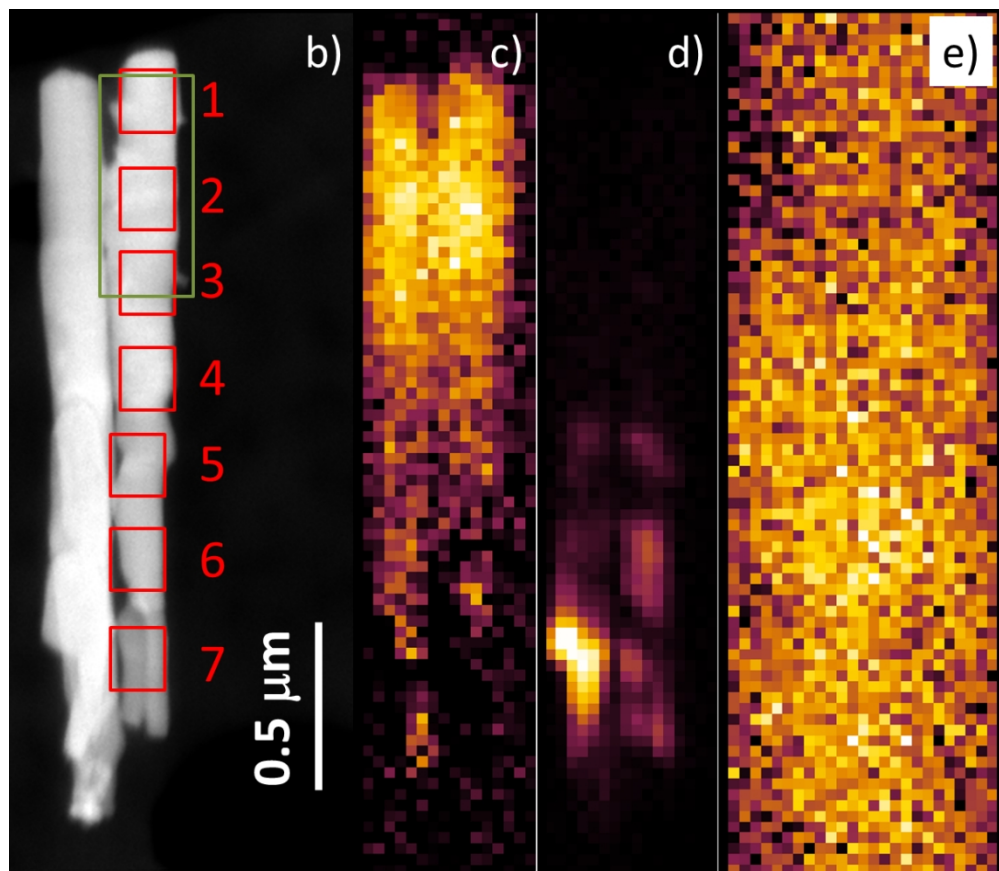


187x107mm (150 x 150 DPI)

1
2
3
4
5
6
7
8
9
10
11
12
13
14
15
16
17
18
19
20
21
22
23
24
25
26
27
28
29
30
31
32
33
34
35
36
37
38
39
40
41
42
43
44
45
46
47
48
49
50
51
52
53
54
55
56
57
58
59
60



196x278mm (96 x 96 DPI)



208x180mm (150 x 150 DPI)

